Scale dependence of local shearing motion in decaying turbulence generated by multiple-jet interaction

Tomoaki Watanabe,[1,2]† Takahiro Mori,[3] Kirari Ishizawa[4] and Koji Nagata[1]

[1]Department of Mechanical Engineering and Science, Kyoto University, Kyoto 615-8540, Japan

[2]Education and Research Center for Flight Engineering, Nagoya University, Nagoya 464-8603, Japan

[3]Department of Aerospace Engineering, Nagoya University, Nagoya 464-8603, Japan

[4]Undergraduate Department of Mechanical and Aerospace Engineering, Nagoya University, Nagoya 464-8603, Japan

(Received xx; revised xx; accepted xx)

Scale dependence of local shearing motion is experimentally investigated in decaying homogeneous isotropic turbulence generated through multiple jet interaction. The turbulent Reynolds number, based on the Taylor microscale, is between approximately 900 and 400. Velocity fields, measured using particle image velocimetry, are analysed through the triple decomposition of a low-pass filtered velocity gradient tensor, which quantifies the intensities of shear and rigid-body rotation at a given scale. These motions manifest predominantly as layer and tubular vortical structures, respectively. The scale dependence of the moments of velocity increments, associated with shear and rigid-body rotation, exhibits power-law behaviours. The scaling exponents for shear are in quantitative alignment with the anomalous scaling of the velocity structure functions, suggesting that velocity increments are predominantly influenced by shearing motion. In contrast, the exponents for rigid-body rotation are markedly smaller than those predicted by Kolmogorov scaling, reflecting the high intermittency of rigid-body rotation. The mean flow structure associated with shear at intermediate scales is investigated with conditional averages around locally intense shear regions in the filtered velocity field. The averaged flow field exhibits a shear layer structure with an aspect ratio of about 4.5, surrounded by rotating motion. The analysis at different scales reveals the existence of self-similar structures of shearing motion across various scales. The mean velocity jump across the shear layer increases with the layer thickness. This relationship is well predicted by Kolmogorov's second similarity hypothesis, which is useful in predicting the mean characteristics of shear layers across a wide range of scales.

† Email address for correspondence: watanabe.tomoaki.8x@kyoto-u.ac.jp

1. Introduction

Fundamental turbulence research explores the scale dependence of turbulent motion in relation to classical turbulence theories (Davidson 2004). The scale dependence is often discussed with the velocity difference Δv between two points separated by a distance r. According to Kolmogorov's second similarity hypothesis, the scaling of velocity structure functions in the inertial subrange is expressed as $\overline{|\Delta v|^n} = \beta_n(\varepsilon r)^{n/3}$, where β_n is a universal constant and ε is the averaged turbulent kinetic energy dissipation rate ε (Kolmogorov 1941). The notation $\overline{f}$ represents the averaging procedure for a variable f. However, discrepancies in this scaling have been reported, with the scaling exponent p of $\overline{|\Delta v|^n} \sim r^p$ becoming progressively smaller than $n/3$ for larger values of n (Kailasnath *et al.* 1992; Castaing *et al.* 1990; Benzi *et al.* 1993; Gauding *et al.* 2021; Iyer *et al.* 2020; Buaria & Sreenivasan 2023). This anomaly in the scaling exponent is attributed to the intermittency at small scales, where eddies at a given scale become less space-filling as the scale decreases. Various corrections to Kolmogorov's original theory have been proposed to account for small-scale intermittency effects (Kolmogorov 1962; She & Leveque 1994; Frisch *et al.* 1978). A comprehensive overview of small-scale intermittency has been provided in Sreenivasan & Antonia (1997) and the references therein.

The velocity gradient tensor $\nabla \boldsymbol{u}$ that describes local fluid motion around a point in space is often used to define turbulent structures, manifesting as coherent patterns in the spatial distribution of physical variables. The symmetric and anti-symmetric parts of $\nabla \boldsymbol{u}$ are the rate-of-strain tensor S_{ij} and the rate-of-rotation tensor Ω_{ij}, respectively, defined as $S_{ij} = [(\nabla \boldsymbol{u})_{ij} + (\nabla \boldsymbol{u})_{ji}]/2$ and $\Omega_{ij} = [(\nabla \boldsymbol{u})_{ij} - (\nabla \boldsymbol{u})_{ji}]/2$. A component of tensors and vectors is specified using subscripts, for example, $(\nabla \boldsymbol{u})_{ij} = \partial u_i/\partial x_j$. At the smallest scale of turbulence characterised by the Kolmogorov scale, vortical structures are often identified using enstrophy, defined as $\omega^2/2 = \Omega_{ij}\Omega_{ij}$. Regions with high $\omega^2/2$ typically concentrate in tubular or sheet-like structures, known respectively as vortex tubes and sheets (Jiménez *et al.* 1993; Vincent & Meneguzzi 1994). Vortex sheets are characterised by local shearing motion, with their defining feature being shear rather than vorticity ω. Consequently, this study calls the sheet-like vortices as shear layers following Eisma *et al.* (2015) and Nagata *et al.* (2020*a*). Numerous identification methods have been developed for vortex tubes, and their properties have been explored in various flow conditions (Jiménez *et al.* 1993; Kang *et al.* 2007; Mouri *et al.* 2007; Ganapathisubramani *et al.* 2008; da Silva *et al.* 2011; Ghira *et al.* 2022). Various turbulence phenomena have been examined in the context of flow associated with vortex tubes, such as turbulent entrainment (Watanabe *et al.* 2017; Neamtu-Halic *et al.* 2021) and particle transport (Matsuda *et al.* 2021).

Recent advancements in the identification of shear layers have been made by adopting the triple decomposition, which separates the velocity gradient tensor into components representing shear (S), rigid-body rotation (R) and elongation (E, or irrotational strain) as $\nabla \boldsymbol{u} = \nabla \boldsymbol{u}_S + \nabla \boldsymbol{u}_R + \nabla \boldsymbol{u}_E$ (Kolář 2007). The triple decomposition is related to the Rortex-based decomposition (Liu *et al.* 2018) and Schur decomposition (Kronborg & Hoffman 2023), although their numerical algorithms were developed independently. Kronborg & Hoffman (2023) demonstrated that triple decomposition is equivalent to the real Schur form of the velocity gradient tensor. The mathematical properties of these decompositions, including Galilean invariance, have been extensively explored in prior research, as well as the theory of Schur decomposition (Wang *et al.* 2018; Keylock 2018). The second and third invariants of $\nabla \boldsymbol{u}$, defined as $Q_{\nabla \boldsymbol{u}} = -(\nabla \boldsymbol{u})_{ij}(\nabla \boldsymbol{u})_{ji}/2$ and $R_{\nabla \boldsymbol{u}} = -(\nabla \boldsymbol{u})_{ij}(\nabla \boldsymbol{u})_{jk}(\nabla \boldsymbol{u})_{ki}/3$, are commonly used to diagnose local flow patterns. The three motions in the triple decomposition can also be identified with $Q_{\nabla \boldsymbol{u}}$ and $R_{\nabla \boldsymbol{u}}$ normalised by the Frobenius norm of $\nabla \boldsymbol{u}$ (Das & Girimaji 2020).

The characteristics of shear layers have been exlored by analysing the shear component of the velocity gradient tensor, $\nabla \boldsymbol{u}_S$. The intensity of local shearing motion can be quantified by the norm of $\nabla \boldsymbol{u}_S$ or the shear component of vorticity vector, $\boldsymbol{\omega}_{Si} = \epsilon_{ijk}(\nabla \boldsymbol{u}_S)_{jk}$, where ϵ_{ijk} is the Levi–Civita symbol (Eisma *et al.* 2015; Nagata *et al.* 2020*a*). By identifying the location and orientation of shear layers using components of $\nabla \boldsymbol{u}_S$, the mean flow field around these layers can be evaluated through a conditional averaging procedure commonly used to investigate coherent structures in turbulence. Previous studies have investigated the mean velocity profiles near shear layers (Eisma *et al.* 2015; Watanabe *et al.* 2020; Fiscaletti *et al.* 2021; Hayashi *et al.* 2021*a*,*b*). A distinct mean velocity jump is observed across the shear layer, with the Kolmogorov scales characterising this jump and the layer thickness in freely evolving turbulence. Recent research highlights the pivotal role of shear layers in turbulent flows. These layers, embedded in a biaxial strain field, contribute significantly to enstrophy production and strain amplification (Watanabe *et al.* 2020). Enoki *et al.* (2023) examined the velocity fields of shear and rigid-body rotation and demonstrated that shearing motion, compared to rigid-body rotation, has a greater impact on the transport of turbulent kinetic energy and energy cascade across scales. The prominence of shear layers over vortex tubes was also confirmed by their contribution to the global enstrophy and mean momentum budget, as shown by the analysis of a reconstructed velocity field from a truncated vorticity field for these structures (Pirozzoli *et al.* 2010). Additionally, the mean flow observed in a strain eigenframe, defined by the eigenvectors of S_{ij}, also exhibits a shear layer pattern even though the average is not taken specifically for the shear layers (Elsinga & Marusic 2010; Elsinga *et al.* 2017; Sakurai & Ishihara 2018). These studies have successfully predicted important properties, including the $-5/3$ law of the energy spectrum and particle transport by turbulence, from the flow observed around shear layers (Elsinga & Marusic 2016; Goudar & Elsinga 2018).

Turbulent structures of various sizes exist although these studies of vortex tubes and shear layers focus on small scales. These structures at intermediate scales, larger than the Kolmogorov scale, can be extracted by applying the vortex identification schemes mentioned earlier to a filtered velocity field $\tilde{\boldsymbol{u}}$, where small-scale velocity fluctuations are removed. In this paper, $\tilde{*}$ denotes a quantity derived from a filtered velocity field. The vortex identification in filtered velocity fields has been conducted with enstrophy $\tilde{\omega}^2/2$ (Leung *et al.* 2012; Goto *et al.* 2017) and the second invariant $\tilde{Q}$ of filtered-velocity gradient tensors (Hirota *et al.* 2017). Leung *et al.* (2012) investigated the morphology of enstrophy isosurfaces in a filtered velocity field using Minkowski functionals. Additionally, tubular vortices have been observed for the isosurfaces of enstrophy of the filtered velocity field (Goto *et al.* 2017). As is the case for vortex tubes and shear layers at the smallest scale, $\tilde{\omega}^2/2$ and $\tilde{Q}$ encounter challenges in distinguishing between vortical structures arising from rigid-body rotation and shear, which are expected to manifest as tubular and sheet-like structures at intermediate scales. Exceptionally, Bermejo-Moreno *et al.* (2009) adapted two local criteria to identify tube and sheet structures at various length scales, although their discussion is primarily confined to the geometry and configuration of these structures.

This study investigates the scale dependence of shearing motion in turbulent flows, leveraging recent advancements in identifying small-scale shear layers. "Small-scale shear layers" in this context refers to the Kolmogorov-scale shear layers identified with fully-resolved velocity gradients. Similar to these small-scale layers, shear layers at intermediate scales may significantly influence the statistical properties of turbulence. The present analysis employs velocity datasets measured using two-component, two-dimensional particle image velocimetry (PIV) in a multiple-jet wind tunnel (Mori *et al.* 2024). This facility generates decaying homogeneous isotropic turbulence with the interaction of high-speed jets. The original PIV data presented in Mori *et al.* (2024) detailed homogeneity, isotropy, stationarity

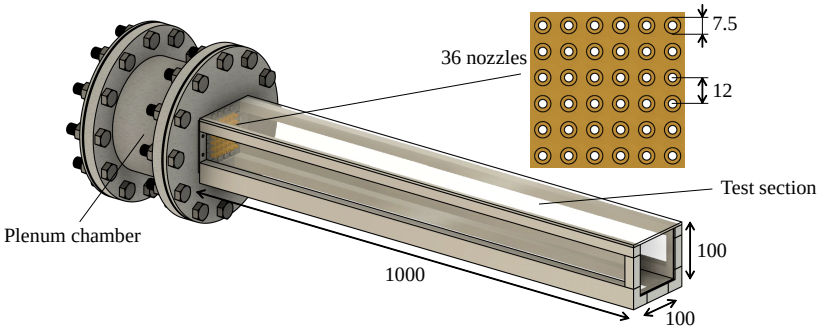

Figure 1: A schematic of a multiple-jet wind tunnel (Mori *et al.* 2024). All dimensions are in mm.

and decay properties using fundamental velocity statistics. A turbulent Reynolds number base on the Taylor microscale ranges from approximately 900 to 400 in the decay region. This study focuses on two key aspects of scale dependence: the scaling of shear intensity moments and the flow structure associated with shearing motion. The first aspect relates to the anomalous scaling in the inertial subrange. We demonstrate that the moment of shear intensity exhibits anomalous scaling similar to that observed in the velocity structure functions, contrasting with the distinct scaling associated with rigid-body rotation found in vortex tubes. For the second aspect, we evaluate conditional averages of shearing motion within the reference frame defined with the shear orientation. Our findings indicate the existence of self-similar structures with shearing motion at intermediate scales, and we show that their mean characteristics align well with Kolmogorov scaling for the inertial subrange. The models of turbulence frequently depict the flow as comprising spatially distributed simple structures (Townsend 1976; Lundgren 1993; Marusic & Monty 2019). The current findings related to the self-similarity of shearing motion are anticipated to be valuable in future efforts to model turbulent flows.

The structure of the paper is as follows. Section 2 describes the experimental facility and the PIV measurements. Section 3 details the post-processing techniques applied to the PIV data, involving scale separation via a low-pass filter, the triple decomposition of the velocity gradient tensor and conditional analysis in the local shear coordinate system. The results are presented in § 4, providing the statistics of shearing motion. The paper concludes in § 5, where the findings are succinctly summarised.

2. Experiments of decaying turbulence generated by high-speed jet interaction

2.1. *Multiple-jet wind tunnel*

The current study analyses velocity data obtained through two-dimensional, two-component PIV in a multiple-jet wind tunnel. The experiments are briefly described here as comprehensive details are available in Mori *et al.* (2024). Figure 1 illustrates the wind tunnel schematic, comprising a plenum chamber and a test section. The plenum chamber features a tubular design with an internal diameter of 330 mm and a length of 180 mm. Its front chamber plate is fitted with 36 Laval nozzles, each having a nozzle outlet diameter of 4.31 mm and a throat diameter of 4.12 mm, with a centre-to-centre distance of 12 mm between adjacent nozzles. Experiments were conducted under a plenum pressure of 200 kPaG, generating ideally expanded supersonic jets with a Mach number of 1.36. This actual Mach number was verified using the Prandtl formula for shock-cell structures visualised in

Schlieren images (Pack 1950), confirming alignment with the design Mach number. The flow in the nozzle becomes choked at plenum pressures exceeding 38.8 kPaG, above which the jet Mach number is not sensitive to the plenum pressure. The back surface of the plenum chamber connects to two air tanks, each with a capacity of 220 L. Dry air is supplied by moisture separators and compressors and stored in these tanks. Each tank is linked to the plenum chamber via a moisture separator, a pressure regulator and a pilot kick 2-port solenoid valve. The pressure regulator is adjusted to maintain a plenum pressure of 200 kPaG.

Compressed air enters the plenum chamber when the valves are opened, initiating the jet flows in the test section. The test section of the wind tunnel is designed with a length of 1000 mm and a square cross-section, each side measuring 100 mm. Optical-grade acrylic plates with a thickness of 1.5 mm are used as the side and bottom walls of the test section. Homogeneous isotropic turbulence is generated through the interaction of jets and subsequently decays along the streamwise direction. The streamwise, vertical and spanwise directions are denoted by x, y and z, respectively, with corresponding velocities u, v and w. The coordinate origin is the centre of the 36 nozzle outlets. The wind tunnel is capable of sustaining a statistically steady turbulent flow for approximately 3 s. This duration is significantly longer than the integral time scale of turbulence, which is typically around 10^{-3} s. Here, the integral time scale of turbulence is defined as the ratio of the integral length scale to the root-mean-squared velocity fluctuations.

2.2. *Measurements*

Velocity measurements were performed using the DANTEC PIV system, which includes a double-pulse Nd:YAG laser (Dantec Dynamics, Dual Power 65-15) and a high-speed camera (Dantec Dynamics, SpeedSense 9070). The camera was equipped with a 105 mm focal length lens (Nikkon, AI AF Micro Nikkor 105mm F2.8D). Light sheet optics attached to the laser generated a thin light sheet with a thickness of less than 1 mm. Both the laser unit and the camera were synchronised and controlled using a synchroniser (Dantec Dynamics, 80N77) and PIV software (Dantec Dynamics, Dynamic Studio). The tracer particles used for PIV were condensed ethanol droplets. In each experiment, 70 ml of liquid ethanol was sprayed into the air tanks, where it evaporated. Air was then compressed and supplied to the tanks. As the ethanol–air mixture passes through the Laval nozzles, the temperature drops due to fluid expansion in the diverging sections, resulting in the ethanol condensation and creating the tracer droplets for the test section. Even in cases of supersaturation, the ethanol mass fraction remains below 1%, ensuring that the condensation has a negligible impact on the turbulent flow in the test section (Clemens & Mungal 1991; Pizzaia & Rossmann 2018). This seeding technique is commonly used in supersonic wind tunnels, employing divergent nozzles to produce supersonic flows. Previous studies have validated the efficacy of this seeding technique, confirming that the generated particles are smaller than 1 μm in diameter. Pizzaia & Rossmann (2018) reported that the diameter of ethanol droplets was approximately 0.05–0.2 μm, and Kouchi *et al.* (2019) used acetone droplets produced by a Laval nozzle for PIV measurement, estimating the droplet diameter at around 160 nm.

The camera, positioned at the side of the test section, captured images of tracer particles illuminated by the laser sheet on the x–y planes at $z = 0$. Particle-pair images were captured at a frequency of 15 Hz and processed using an adaptive PIV algorithm (Theunissen 2010) and universal outlier detection (Westerweel & Scarano 2005), as implemented in Dynamic Studio. The interrogation area for the adaptive PIV algorithm ranges from a minimum of 16×16 pixels to a maximum of 32×32 pixels. Our previous study reported PIV measurements conducted at six different streamwise locations, centred at $x = 0.150$ m, 0.267 m, 0.360 m, 0.465 m, 0.605 m and 0.746 m (Mori *et al.* 2024). The flow is highly inhomogeneous in the cross-section at the first two measurement stations. Homogeneous isotropic turbulence decays

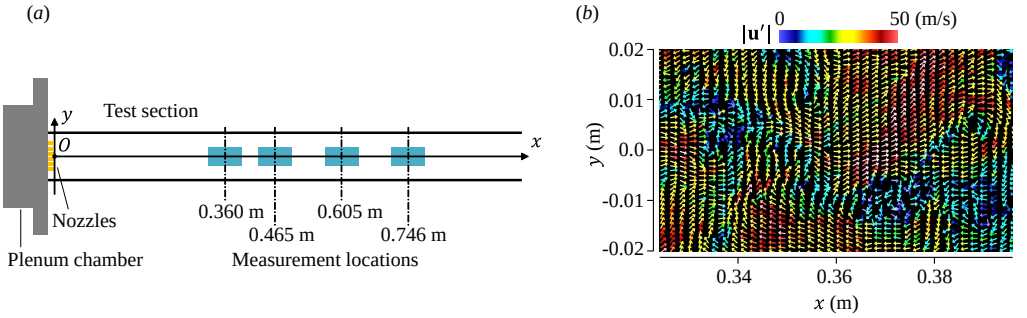

Figure 2: (a) Measurement locations for PIV. (b) An example of velocity fluctuation vectors $\boldsymbol{u}' = (u', v')$ measured by PIV. The colour represents the magnitude of the vectors, $|\boldsymbol{u}'|$.

from the measurement station of $x = 0.360$ m. Therefore, the present study analyses velocity fields measured at $x = 0.360$ m, 0.465 m, 0.605 m and 0.746 m. The time interval between two laser pulses was set at 4 μs. The measurement area covered approximately 70 mm in the streamwise direction and 40 mm in the vertical direction, with a spatial resolution (vector spacing) of about 1 mm in both directions. Figure 2(a) illustrates the measurement locations and the field of view in the homogeneous and isotropic region. In each wind tunnel run, an average of 30 velocity vector snapshots were captured by the PIV. The experiments were repeated until approximately 600 velocity vector profiles were obtained at each measurement location. Velocity statistics are calculated using ensemble averages and averages in the y direction as functions of x. The averages of any variable f are denoted by $\overline{f}$, with the fluctuations represented as $f' = f - \overline{f}$. Figure 2(b) visualises the flow field with velocity fluctuation vectors (u', v') measured around $x = 0.360$ m. At this location, the mean flow from the jet nozzles leaves no imprints due to the interaction of multiple jets.

Our previous study presented fundamental velocity statistics of turbulence, such as mean velocity, root-mean-squared (rms) velocity fluctuations, auto-correlation functions and energy spectra (Mori *et al.* 2024). The accuracy of the PIV measurements was validated by comparing the energy spectra, auto-correlation functions and non-dimensional energy dissipation rate with those of other incompressible turbulence and by comparing the turbulence-induced Pitot pressure (Bailey *et al.* 2013) with velocity variances measured by the PIV. The spatial resolution of the PIV is close to the Taylor microscale, and spectral analysis has confirmed that scales larger than the small-scale end of the inertial subrange are well-resolved by the PIV. The scale dependence of velocity fluctuations in these resolved scales is considered accurately measured, as suggested by comparisons of energy spectra with other turbulent flows (Mori *et al.* 2024). Similar approaches to investigating turbulent structures at intermediate scales using under-resolved PIV have been reported in other studies, such as Coriton *et al.* (2014). Spatial distributions of various velocity statistics indicate that the flow is statistically homogeneous and isotropic for $x \gtrsim 0.35$ m. Additionally, mean static pressure and temperature were measured along the centreline of the test section.

Although the jets emanating from the nozzles are supersonic, they rapidly mix with the low-speed ambient fluid, leading to a rapid decay in mean velocity before homogeneous isotropic turbulence develops due to jet interaction. Consequently, the flow transitions to a subsonic regime before turbulence begins to decay. Beyond $x = 0.35$ m, the mean flow Mach number $M = \overline{u}/a$ is approximately 0.1, with the turbulent Mach number $M_T = \sqrt{\overline{u'^2} + 2\overline{v'^2}}/a$ being even lower, under 0.1, where a is the speed of sound. Additionally, the mean temperature

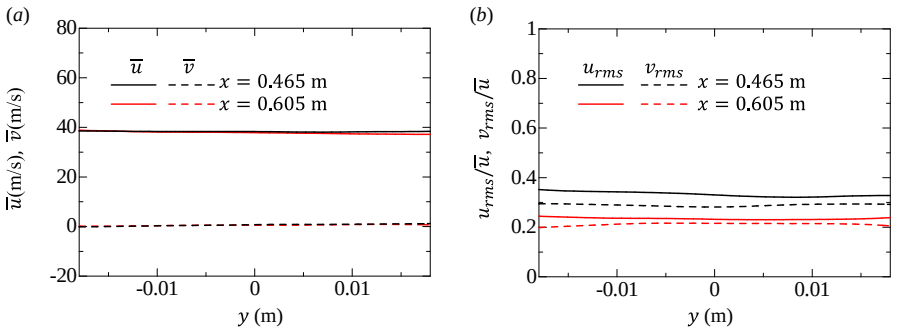

Figure 3: Vertical profiles of (a) mean velocity and (b) turbulence intensity at $x = 0.465$ m and $x = 0.605$ m.

and density in the decay region remain constant at $T = 303$ K and $\rho = 1.16$ kg/m^3, respectively, without streamwise variations. As a result of these conditions, compressibility effects are locally negligible in the decay region of homogeneous isotropic turbulence. However, it is important to note that the findings of this study may not be restricted to incompressible turbulence alone, as both compressible and incompressible turbulences share the same dynamical properties described by the Navier–Stokes equations.

2.3. *Decay properties*

Some fundamental velocity statistics in turbulence generated by jet interaction are presented here, with further details on flow characteristics available in Mori *et al.* (2024). Figure 3(a) shows the vertical profiles of mean velocity, $\overline{u}$ and $\overline{v}$, in the streamwise and vertical directions at two measurement locations. The mean streamwise velocity is approximately 39 m/s, consistent across the vertical direction. The vertical mean velocity is negligibly small, indicating a uniform mean flow in the wind tunnel. Figure 3(b) presents the turbulence intensity, defined by the root-mean-square (rms) velocity fluctuations, $u_{rms} = \sqrt{\overline{u'^2}}$ and $v_{rms} = \sqrt{\overline{v'^2}}$, normalised by the mean velocity $\overline{u}$. The turbulence intensity decreases in the streamwise direction, reflecting the decay of the turbulence, yet remains uniformly distributed in the vertical direction for both velocity components. The turbulence intensity at these two streamwise locations exceeds 0.2, a value higher than that typically observed in grid turbulence, where turbulence intensity is usually less than 0.05 (Melina *et al.* 2016; Nagata *et al.* 2017). The high turbulence intensity in this experiment is attributed to the nature of turbulence generated by jet interaction (Tan *et al.* 2023). The ratio of the rms velocity fluctuations, u_{rms}/v_{rms}, is about 1.1, aligning with values reported for turbulence generated by grids and multiple-jet interactions (Krogstad & Davidson 2012; Isaza *et al.* 2014; Kitamura *et al.* 2014; Watanabe & Nagata 2018; Tan *et al.* 2023). Consequently, the nearly homogeneous and isotropic turbulence generated by the jets decays in the test section.

Figure 4(a) illustrates the streamwise decay of turbulent kinetic energy per unit mass k_T, within the homogeneous isotropic region, calculated as $k_T = (\overline{u'^2} + 2\overline{v'^2})/2$. In decaying isotropic turbulence, such as that observed in grid turbulence, the decay of k_T is commonly approximated by a power law $k_T = a_k(x - x_0)^{-n_k}$ with a coefficient a_k, a virtual origin x_0 and a decay exponent n_k (Mohamed & Larue 1990; Davidson 2004). The Levenberg–Marquardt method was employed to simultaneously determine these three parameters from the measured k_T values (Mori *et al.* 2024). The analysis yielded $a_k = 21.0\,\mathrm{m^2/s^2}$, $x_0 = 0.12$ m

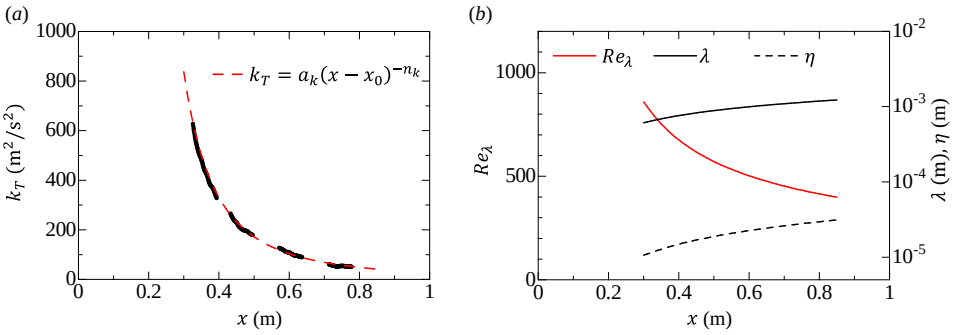

Figure 4: The decay properties of turbulence generated by the jet interaction measured in Mori *et al.* (2024): (*a*) turbulent kinetic energy per unit mass, $k_T = (\overline{u'^2} + 2\overline{v'^2})/2$, and (*b*) Taylor microscale, Kolmogorov scale and turbulent Reynolds number. A power law $k_T = a_k(x - x_0)^{-n_k}$ is compared with the measured data in (*a*).

and $n_k = 2.1$. The power law effectively approximates the decay of k_T in figure 4(*a*). Notably, the exponent n_k is higher than the typical values observed in grid turbulence.

Since the turbulence is statistically homogeneous within the cross-sectional plane, the decay of the turbulent kinetic energy per unit mass, k_T, is directly related to its dissipation rate ε. This relationship can be mathematically expressed as:

$$\varepsilon = -\overline{u}\frac{\partial k_T}{\partial x} = \overline{u}a_k n_k (x - x_0)^{-n_k - 1}. \tag{2.1}$$

This formula is frequently employed to evaluate the dissipation rate in grid turbulence, as the mean velocity, $\overline{u}$, and k_T are typically more straightforward to measure than the dissipation rate ε itself (Kistler & Vrebalovich 1966; Thormann & Meneveau 2014). The energy spectrum within the inertial subrange, when normalised by the dissipation rate estimated using (2.1), has been shown to agree with results from other incompressible turbulent flows (Mori *et al.* 2024).

The turbulent Reynolds number Re_λ and Kolmogorov scale η are evaluated as $Re_\lambda = \sqrt{2k_T/3}\lambda/\nu$ and $\eta = \nu^{3/4}\varepsilon^{-1/4}$. Here, $\lambda = \sqrt{10\nu k_T/\varepsilon}$ is the Taylor microscale and $\nu = \mu/\rho$ is the kinematic viscosity (μ is the viscosity coefficient). Figure 4(*b*) displays the streamwise variations of λ, η and Re_λ. The Reynolds number varies approximately between 900 and 400. The Taylor microscale is estimated to be around 1 mm, which is close to the spatial resolution of the PIV. In addition, the Kolmogorov velocity and time scales are defined respectively as $u_\eta = (\nu\varepsilon)^{1/4}$ and $\tau_\eta = (\nu/\varepsilon)^{1/2}$. These scales are utilised to normalise the statistics of shearing motions.

Figure 5 presents the longitudinal energy spectra of streamwise and vertical velocities, $E_u(k_x)$ and $E_v(k_y)$, at $x = 0.605$ m, where k_x and k_y represent the wavenumbers in the x and y directions, respectively. The spectra and wavenumbers are normalised using ε, ν and η to facilitate comparison with other turbulent flows. The measurement area and spatial resolution of the PIV determine the lowest and highest wavenumbers. Within the available range, the spectra follow $E_u \sim k_x^{-5/3}$ and $E_v \sim k_y^{-5/3}$, as expected for the inertial subrange. Additionally, the normalised spectra quantitatively align with those from other studies, further confirming the full development of turbulence. An inset in the figure displays the ratio of energy spectra, E_u/E_v, providing a scale-dependent measure of statistical isotropy. The ratio is about 1.08 across all wavenumbers, indicating that the velocity fluctuations at each scale are approximately statistically isotropic.

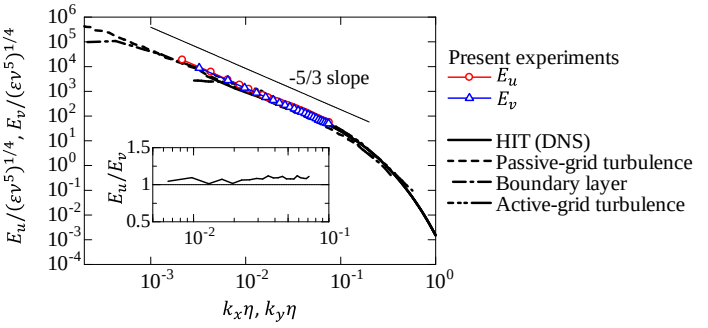

Figure 5: Normalised longitudinal energy spectra of streamwise and vertical velocities, $E_u(k_x)$ and $E_v(k_y)$, measured at $x = 0.605$m, where k_x and k_y represent the wavenumbers in the x and y directions, respectively. For comparison, the figure also includes energy spectra from DNS of homogeneous isotropic turbulence (HIT) with $Re_\lambda = 202$ (Watanabe & Nagata 2023) and from experiments of passive-grid turbulence with $Re_\lambda = 520$ (Kistler & Vrebalovich 1966), a boundary layer with $Re_\lambda = 1450$ (Saddoughi & Veeravalli 1994; Nieuwstadt & Boersma 2016) and active-grid turbulence with $Re_\lambda = 241$ (Zheng *et al.* 2021).

Table 1: Summary of turbulence characteristics: the turbulent Reynolds number Re_λ; the characteristic velocity scale of large-scale motions $\mathcal{U} = \sqrt{2k_T/3}$; the Kolmogorov velocity scale u_η; the integral scale L_u; the Taylor microscale λ ; the Kolmogorov scale η; the spatial resolution of PIV Δ; the integral time scale $T = L_u/\mathcal{U}$; the Kolmogorov time scale τ_η.

Measurement location x (m)	0.360	0.465	0.605	0.746
Re_λ	732	600	498	433
$\mathcal{U}$ (m/s)	16.7	11.4	8.0	6.1
u_η (m/s)	1.22	0.92	0.71	0.58
L_u (m)	0.022	0.024	0.028	0.026
λ (m)	7.1×10^{-4}	8.5×10^{-4}	1.0×10^{-4}	1.1×10^{-3}
η (m)	1.3×10^{-5}	1.8×10^{-5}	2.3×10^{-5}	2.8×10^{-5}
Δ (m)	9.5×10^{-4}	8.9×10^{-4}	9.2×10^{-4}	9.1×10^{-4}
T (s)	1.3×10^{-3}	2.1×10^{-3}	3.4×10^{-3}	4.2×10^{-3}
τ_η (s)	1.1×10^{-5}	1.9×10^{-5}	3.2×10^{-5}	4.8×10^{-5}
L_u/η	1635	1390	1207	932
λ/η	53.3	48.2	43.9	40.9
$\mathcal{U}/u_\eta$	13.8	12.5	11.3	10.6
T/τ_η	119	112	106	88

Table 1 summarises the turbulence characteristics at the centre of each PIV measurement area. Here, $\mathcal{U} = \sqrt{2k_T/3}$ represents the characteristic velocity scale of large-scale motions, L_u is the integral scale evaluated using the longitudinal auto-correlation function of streamwise velocity and $T = L_u/\mathcal{U}$ is the integral time scale.

3. Scale-dependent analysis of shearing motion

3.1. *Low-pass filtered velocity field*

The scale dependence of shearing motion is explored with the PIV data. The present approach involves examining local fluid motion through a coarse-grained velocity gradient, defined as the gradient of a low-pass filtered velocity field. The low-pass filter applied to the two-dimensional components of the velocity vector (u, v) measured on an x–y plane is characterised by a filter Kernel function $G(r)$:

$$\tilde{u}(x, y) = \iint u(x', y')G(r, L_f)dx'dy', \tag{3.1}$$

$$\tilde{v}(x, y) = \iint v(x', y')G(r, L_f)dx'dy', \tag{3.2}$$

$$r = \sqrt{(x' - x)^2 + (y' - y)^2}, \tag{3.3}$$

where the integration is calculated over the entire field of view, and L_f is the cutoff length scale of the filter. We utilise the Gaussian filter (Pope 2000), with $G(r)$ given by

$$G(r, L_f) = \sqrt{\frac{6}{\pi L_f^2}} \exp\left(\frac{-6r^2}{L_f^2}\right). \tag{3.4}$$

The integral ranges of x' and y' in (3.1) and (3.2) extend over a length of $2L_f$, specifically defined as $-C_f L_f \leqslant x' - x \leqslant C_f L_f$ and $-C_f L_f \leqslant y' - y \leqslant C_f L_f$ with $C_f = 1$. At the distance $r = L_f$, the Gaussian function G is less than 0.25% of its peak value at $r = 0$. Extending the integral ranges beyond this does not influence the results. This has been verified by performing the analyses described in this paper with $C_f = 1, 2$ and 3. In this paper, $\tilde{f}$ denotes a quantity f defined with the filtered velocity field of (3.1, 3.2). For instance, the vorticity of the filtered velocity field is $\tilde{\omega} = \partial\tilde{v}/\partial x - \partial\tilde{u}/\partial y$. The analysis described below has also been conducted using direct numerical simulation (DNS) databases of incompressible isotropic turbulence (Watanabe & Nagata 2023), where different filters are tested. It has been confirmed that similar results are obtained with both the Gaussian filter and a sharp spectral filter (described by a top-hat transfer function in Fourier space) (Pope 2000). However, a box filter, defined as a top-hat function of $G(r)$, has led to unphysical results due to oscillations in the transfer function in wavenumber space (Pope 2000).

The statistics of the filtered velocity are evaluated for a range of the filter length L_f. This filter length is determined relative to the spatial resolution of the PIV, Δ, as $L_f = C_L\Delta$. The coefficient C_L varies in the range of 4.8 and 9.2. The maximum value of L_f is less than a half of the integral scale of the turbulence. Conversely, the minimum value of L_f is greater than 140η. Using the same PIV data, Mori *et al.* (2024) have demonstrated that the energy spectra follow the $-5/3$ law across the wavenumber range corresponding to L_f/η examined in this study.

3.2. *The triple decomposition of the coarse-grained velocity gradient tensor*

The triple decomposition of the velocity gradient tensor is applied to the filtered velocity $(\tilde{u}, \tilde{v})$. This approach follows the methodology outlined in Eisma *et al.* (2015), where the triple decomposition was similarly applied to two-dimensional and two-component PIV data of a turbulent boundary layer. Three-dimensional turbulent motions are described on two-dimensional planes, where out-of-plane motions are not accurately captured. This limitation is anticipated based on previous studies of flow topology (Perry & Chong 1994; Rabey *et al.* 2015). The disparity between the triple decompositions of two- and three-

dimensional velocity gradient tensors is examined with DNS of homogeneous isotropic turbulence in appendix A. The present experimental analysis is also conducted on nearly homogeneous isotropic turbulence generated by jet interaction. It is demonstrated that the intensities of the motions considered in the triple decomposition are underestimated on two-dimensional planes due to the absence of out-of-plane motions. However, the scale dependence of the intensities of decomposed motions is similar for both two- and three-dimensional decompositions. Thus, the analysis using the triple decomposition on two-dimensional planes still offers valuable insights into local turbulent motions.

The velocity gradient of $(\tilde{u}, \tilde{v})$ characterises local fluid motion at a specific point (x, y) and a scale determined by the filter length L_f. The two-dimensional velocity gradient tensor $\nabla\tilde{\boldsymbol{u}}$ is represented as

$$\nabla\tilde{\boldsymbol{u}} = \begin{pmatrix} \partial\tilde{u}/\partial x & \partial\tilde{u}/\partial y \\ \partial\tilde{v}/\partial x & \partial\tilde{v}/\partial y \end{pmatrix}. \tag{3.5}$$

As introduced earlier, the triple decomposition splits the velocity gradient tensor into three components: shear (S), rigid-body rotation (R) and elongation (E), formulated as $\nabla\tilde{\boldsymbol{u}} = \nabla\tilde{\boldsymbol{u}}_S + \nabla\tilde{\boldsymbol{u}}_R + \nabla\tilde{\boldsymbol{u}}_E$. The decomposition algorithm is the same as in Kolář (2007) and Eisma *et al.* (2015) and is briefly explained herein. For a deeper understanding of the physical meaning and mathematical properties of this decomposition, readers can refer to the previous studies on the triple decomposition, as discussed in § 1.

The application of the triple decomposition begins with searching for a basic reference frame, which is defined at each position. This reference frame is determined by the eigenvectors of the rate of strain tensor $\tilde{S}_{ij} = [(\nabla\tilde{\boldsymbol{u}})_{ij} + (\nabla\tilde{\boldsymbol{u}})_{ji}]/2$. The eigenvalues of $\tilde{S}_{ij}$ are denoted as s_1 and s_2 , where $s_1 \geqslant s_2$. The corresponding eigenvectors are $\boldsymbol{e}_1 = (e_{1x}, e_{1y})$ and $\boldsymbol{e}_2 = (e_{2x}, e_{2y})$, respectively. Here, e_{nx} and e_{ny} represent the x and y components of $\boldsymbol{e}_n$ for $n = 1$ or 2. The transformation matrix $\boldsymbol{Q}_e$ that converts coordinates from the laboratory coordinate $\boldsymbol{x} = (x, y)$ to the reference frame $\boldsymbol{x}_e$ of the principal axes, defined by the eigenvectors $\boldsymbol{e}_1$ and $\boldsymbol{e}_2$, is expressed as:

$$\boldsymbol{Q}_e = \begin{pmatrix} e_{1x} & e_{1y} \\ e_{2x} & e_{2y} \end{pmatrix}. \tag{3.6}$$

The basic reference frame is obtained by rotating the coordinate system $\boldsymbol{x}_e = \boldsymbol{Q}_e\boldsymbol{x}$ by $\theta = 45°$. The rotational transformation matrix $\boldsymbol{Q}_r(\theta)$ is given by

$$\boldsymbol{Q}_r(\theta) = \begin{pmatrix} \cos\theta & \sin\theta \\ -\sin\theta & \cos\theta \end{pmatrix}. \tag{3.7}$$

Consequently, the coordinate transformation from the laboratory coordinate to the basic reference frame is expressed as $\boldsymbol{Q}_b = \boldsymbol{Q}_r(45°)\boldsymbol{Q}_e$. The filtered velocity gradient tensor in the basic reference frame, denoted as $\nabla\tilde{\boldsymbol{u}}^{(b)}$, is calculated as $\nabla\tilde{\boldsymbol{u}}^{(b)} = \boldsymbol{Q}_b\nabla\tilde{\boldsymbol{u}}\boldsymbol{Q}_b^T$, where the superscript (b) indicates quantities evaluated in the basic reference frame and $\boldsymbol{Q}_b^T$ is the transposed matrix of $\boldsymbol{Q}_b$. Subsequently, $\nabla\tilde{\boldsymbol{u}}^{(b)}$ is decomposed into three components, $\nabla\tilde{\boldsymbol{u}}_S^{(b)}$, $\nabla\tilde{\boldsymbol{u}}_R^{(b)}$ and $\nabla\tilde{\boldsymbol{u}}_E^{(b)}$, in the basic reference frame as follows:

$$(\nabla\tilde{\boldsymbol{u}}_{RES}^{(b)})_{ij} = \mathrm{sgn}\left[(\nabla\tilde{\boldsymbol{u}}^{(b)})_{ij}\right] \min\left[\left|(\nabla\tilde{\boldsymbol{u}}^{(b)})_{ij}\right|, \left|(\nabla\tilde{\boldsymbol{u}}^{(b)})_{ji}\right|\right], \tag{3.8}$$

$$(\nabla\tilde{\boldsymbol{u}}_S^{(b)})_{ij} = (\nabla\tilde{\boldsymbol{u}}^{(b)})_{ij} - (\nabla\tilde{\boldsymbol{u}}_{RES}^{(b)})_{ij}, \tag{3.9}$$

$$(\nabla\tilde{\boldsymbol{u}}_R^{(b)})_{ij} = \left[(\nabla\tilde{\boldsymbol{u}}_{RES}^{(b)})_{ij} - (\nabla\tilde{\boldsymbol{u}}_{RES}^{(b)})_{ji}\right]/2, \tag{3.10}$$

$$(\nabla\tilde{\boldsymbol{u}}_E^{(b)})_{ij} = \left[(\nabla\tilde{\boldsymbol{u}}_{RES}^{(b)})_{ij} + (\nabla\tilde{\boldsymbol{u}}_{RES}^{(b)})_{ji}\right]/2, \tag{3.11}$$

for $i, j = 1$ and 2, where sgn is the sign function. Here, $\nabla\tilde{\boldsymbol{u}}_{RES}$, referred to as the residual tensor, is the remnant from $\nabla\tilde{\boldsymbol{u}}$ after extracting shear $\nabla\tilde{\boldsymbol{u}}_S$. Finally, the components of shear, rigid-body rotation and elongation in the original coordinate system are obtained by applying the inverse transformation of $\boldsymbol{Q}_b$, $\boldsymbol{Q}_b^{-1} = \boldsymbol{Q}_b^T$, as $\nabla\tilde{\boldsymbol{u}}_\alpha = \boldsymbol{Q}_b^T \nabla\tilde{\boldsymbol{u}}_\alpha^{(b)} \boldsymbol{Q}_b$ for $\alpha =$ S, R and E.

The intensities of shear and rigid-body rotation are defined using the norm of the decomposed velocity gradient tensors as $\tilde{I}_S = \sqrt{2(\nabla\tilde{\boldsymbol{u}}_S)_{ij}(\nabla\tilde{\boldsymbol{u}}_S)_{ij}}$ and $\tilde{I}_R = \sqrt{2(\nabla\tilde{\boldsymbol{u}}_R)_{ij}(\nabla\tilde{\boldsymbol{u}}_R)_{ij}}$ (Hayashi *et al.* 2021*a*). The vorticity vector of filtered velocity, $\tilde{\omega} = \partial\tilde{v}/\partial x - \partial\tilde{u}/\partial y$, is decomposed into two components corresponding to shear and rigid-body rotation: $\tilde{\omega} = \tilde{\omega}_S + \tilde{\omega}_R$. The shear vorticity $\tilde{\omega}_S$ and the vorticity of rigid-body rotation $\tilde{\omega}_R$ are defined as $\tilde{\omega}_S = (\nabla\tilde{\boldsymbol{u}}_S)_{21} - (\nabla\tilde{\boldsymbol{u}}_S)_{12}$ and $\tilde{\omega}_R = (\nabla\tilde{\boldsymbol{u}}_R)_{21} - (\nabla\tilde{\boldsymbol{u}}_R)_{12}$. The magnitude of $\tilde{\omega}_S$ and $\tilde{\omega}_R$ is related to the intensity of the corresponding motion as $\sqrt{2}|\tilde{\omega}_S| = \tilde{I}_S$ and $|\tilde{\omega}_R| = \tilde{I}_R$. For the fully-resolved velocity gradient tensor $\nabla\boldsymbol{u}$, I_S and I_R are associated with shear layers (vortex sheets) and vortex tubes with sizes of the Kolmogorov scale, respectively. For this reason, the present study focuses on these two motions, for which the statistics of $\tilde{I}_S$ and $\tilde{I}_R$ are evaluated at various length scales.

3.3. *The analysis of flow structures associated with shearing motion*

The flow structure associated with shearing motion in the filtered velocity fields is explored using a conditional-averaging procedure. This method involves taking averages around regions exhibiting locally intense shear within a local reference frame that is oriented according to the direction of the shear. This approach aligns with the methodologies previously employed for investigating small-scale shear layers identified with the fully-resolved velocity gradient tensor (Eisma *et al.* 2015; Watanabe *et al.* 2020; Hayashi *et al.* 2021*a*; Fiscaletti *et al.* 2021; Watanabe & Nagata 2022). As such, the techniques previously used to study small-scale shear layers are adapted and applied to the filtered velocity field.

The initial step is to identify locations of locally intense shear within the filtered velocity field. Following Hayashi *et al.* (2021*a*) and Fiscaletti *et al.* (2021), the present study analyses flow around points where two conditions are met: firstly, the shear intensity $\tilde{I}_S$ reaches a local maximum, and secondly $\tilde{I}_S$ exceeds a threshold, denoted as I_{Sth}. The shear layer exhibits a high shear intensity at its centre, as observed in the spatial distribution of shear intensity, and this central location can be identified as the local maximum of shear intensity (Hayashi *et al.* 2021*a*; Fiscaletti *et al.* 2021). Additionally, the local maximum of shear intensity can be detected even in regions of very weak shear, which may be partially attributed to measurement errors. To mitigate this issue, these regions of weak shear are excluded by applying a threshold. This threshold to analyse small-scale shear layers was previously implemented in Fiscaletti *et al.* (2021), where the threshold dependence was also addressed. In the present study, the threshold is defined as $I_{Sth} = C_{th}\overline{\tilde{I}_S}$, where C_{th} is a constant. We adopt $C_{th} = 1.5, 2.0, 2.5, 3.0$ and 3.5 to examine C_{th} dependence.

The second step is identifying a local reference frame that characterises the shear orientation. This frame is referred to as a shear coordinate, denoted by $\boldsymbol{x}_s = (\zeta_1, \zeta_2)$, where quantities are represented with a superscript (s). The shear coordinate is defined such that the shear component $\nabla\tilde{\boldsymbol{u}}_S$ in this coordinate system takes the following form:

$$\nabla\tilde{\boldsymbol{u}}_S^{(s)} = \begin{pmatrix} 0 & |\omega_S| \\ 0 & 0 \end{pmatrix}. \tag{3.12}$$

To establish the transformation matrix $\boldsymbol{Q}_s$ from the laboratory coordinate to the shear coordinate, we utilise the matrix $\boldsymbol{Q}_b$ for the basic reference frame. The matrix $\boldsymbol{Q}_s$ is defined

as $\boldsymbol{Q}_s = \boldsymbol{Q}_2\boldsymbol{Q}_1\boldsymbol{Q}_b$, where $\boldsymbol{Q}_1$ and $\boldsymbol{Q}_2$ are given by:

$$\boldsymbol{Q}_1 = \begin{cases} \boldsymbol{Q}_r(90^\circ) & \text{when } \left|\left(\nabla\tilde{\boldsymbol{u}}_S^{(b)}\right)_{12}\right| = 0 \\ \boldsymbol{I} & \text{otherwise} \end{cases}, \tag{3.13}$$

and

$$\boldsymbol{Q}_2 = \begin{cases} \boldsymbol{Q}_{sym} & \text{when } \left|\left(\boldsymbol{Q}_1\nabla\tilde{\boldsymbol{u}}_S^{(b)}\right)_{12}\right| < 0 \\ \boldsymbol{I} & \text{otherwise} \end{cases}, \tag{3.14}$$

where $\boldsymbol{I}$ is the identity tensor and $\boldsymbol{Q}_{sym}$ is a symmetric transformation matrix written as:

$$\boldsymbol{Q}_{sym} = \begin{pmatrix} 1 & 0 \\ 0 & -1 \end{pmatrix}. \tag{3.15}$$

This derivation of $\boldsymbol{Q}_s$ is based on the characteristics of $\nabla\tilde{\boldsymbol{u}}_S$, which has only one non-zero component in the basic reference frame, either $(\nabla\tilde{\boldsymbol{u}}_S^{(b)})_{12}$ or $(\nabla\tilde{\boldsymbol{u}}_S^{(b)})_{21}$ (Kolář 2007). In the shear coordinate, the shear relates to flows in the $-\zeta_1$ direction for $\zeta_2 > 0$ and in the ζ_1 direction for $\zeta_2 < 0$.

Finally, ensemble averages of all local maxima of $\tilde{I}_S$ are evaluated in the shear coordinate. At each local maximum of $\tilde{I}_S$, the shear coordinate $\boldsymbol{x}_s = (\zeta_1, \zeta_2)$ is given by $\boldsymbol{x}_s = \boldsymbol{Q}_s\boldsymbol{x}$. The shear coordinate is discretised using the following function:

$$\zeta_i(n) = -\frac{\zeta_{max}}{\alpha_\zeta}\mathrm{atanh}\left[\tanh(\alpha_\zeta)\left(1 - \frac{n + N_\zeta}{N_\zeta}\right)\right], \tag{3.16}$$

where $n = -N_\zeta, \ldots, N_\zeta$ is an integer specifying discrete points, $N_\zeta = 60$ determines the resolution, $\alpha_\zeta = 2.5$ is a stretching parameter, and $\zeta_{max} = 7.5L_f$ defines the range of ζ_i as $-\zeta_{max} \leqslant \zeta_i \leqslant \zeta_{max}$. The spacing between discrete points decreases as $|\zeta_i|$ approaches zero, providing enhanced spatial resolution near the shear layer where the velocity gradient is large. This function has also been employed for spatial discretisation in DNS, and the distribution of discrete points has been detailed in previous studies (Watanabe *et al.* 2018; Akao *et al.* 2022). The velocity vector in the shear coordinate, $\tilde{\boldsymbol{u}}^{(s)} = (\tilde{u}_1^{(s)}, \tilde{u}_2^{(s)})$, is calculated as $\tilde{\boldsymbol{u}}^{(s)} = \boldsymbol{Q}_s\tilde{\boldsymbol{u}}$. Furthermore, the shear vorticity in the shear coordinate, $\tilde{\omega}_S^{(s)}$, is determined using the shear tensor in the shear coordinate $\nabla\tilde{\boldsymbol{u}}_S^{(s)} = \boldsymbol{Q}_s\nabla\tilde{\boldsymbol{u}}_S\boldsymbol{Q}_s^T$. Other vectors and tensors in the shear coordinate are evaluated in this manner using $\boldsymbol{Q}_s$. For the velocity vectors, the relative velocity with respect to $(\zeta_1, \zeta_2) = (0, 0)$ is analysed to reveal the local flow pattern around shearing motion. These quantities are evaluated on the discrete shear coordinate by interpolating the PIV data in the laboratory coordinate system. The present study employs a third-order Lagrange polynomial interpolation scheme. For each local maximum of $\tilde{I}_S$, this procedure computes the variable f as a function of (ζ_1, ζ_2), where the range of (ζ_1, ζ_2) is confined within the measurement area of PIV. Consequently, no extrapolation of the PIV data is utilised in the analysis of the shear layer. Thus, the number of statistical samples varies depending on the location on (ζ_1, ζ_2). The ensemble average of f is then computed as a function of (ζ_1, ζ_2) with all local maxima of $\tilde{I}_S$. This average is denoted by $\langle f \rangle$.

4. Results and Discussion

4.1. *Intensities of shearing motion and rigid-body rotation*

Figure 6 visualises the instantaneous intensities of rigid-body rotation, $\tilde{I}_R$, and shear, $\tilde{I}_S$, in the filtered velocity field at the PIV measurement centred at $x = 0.360$ m. The filter length is set at $L_f/\eta = 343$. The distribution of $\tilde{I}_R$ is highly intermittent in space. Most

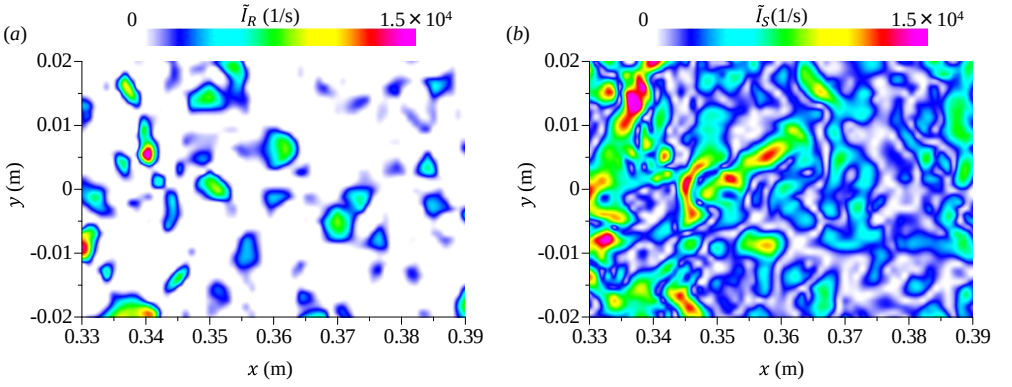

Figure 6: Distributions of the intensities of (a) rigid-body rotation $\tilde{I}_R$ and (b) shear $\tilde{I}_S$ in a filtered velocity field with a filter length $L_f/\eta = 343$.

parts of the flow exhibit $\tilde{I}_R \approx 0$, with large $\tilde{I}_R$ values concentrated in small, discrete spots. These large values of $\tilde{I}_R$, often circular in shape, are indicative of vortex tubes with axes perpendicular to the measurement plane. Smaller but non-zero values of $\tilde{I}_R$ do not always have a circular shape but exhibit an elliptic shape elongated in one direction. These regions possibly indicate vortex tubes with axes nearly parallel to the measurement planes. As the out-of-plane component of rigid-body rotation is not captured on the two-dimensional plane, $\tilde{I}_R$ for these vortices can be underestimated by the analysis of two-dimensional velocity fields, as confirmed in appendix A. Shearing motion, represented by $\tilde{I}_S > 0$, is almost everywhere throughout the flow. Consequently, turbulent motion at intermediate scales is predominantly governed by shear. While $\tilde{I}_R$ and $\tilde{I}_S$ are related to turbulent motions at intermediate scales, their spatial distributions are consistent with rigid-body rotation and shear at the smallest scales, where the former is intermittently present at the smallest scales while the latter is more pervasive than rigid-body rotation (Hayashi *et al.* 2021*a*). The predominance of shearing motion at the smallest scales has been consistently reported for various turbulent flows in analyses employing the three-dimensional triple decomposition, and this observation is unlikely to be influenced by the two-dimensional triple decomposition (Nagata *et al.* 2020*a*; Das & Girimaji 2020; Hayashi *et al.* 2021*a*). This tendency persists even in random velocity fields, which are not solutions to the Navier–Stokes equations (Watanabe & Nagata 2022). Thus, the highly intermittent nature of rigid-body rotation is considered a kinematic characteristic of fluctuating velocity fields.

Figure 7 displays the mean intensities of shear and rigid-body rotation, $\overline{\tilde{I}_S}$ and $\overline{\tilde{I}_R}$, as functions of the filter length L_f. The mean intensities and L_f are normalised by the Kolmogorov time and length scales, respectively. These experimental results are presented with data from a DNS database of statistically steady, homogeneous and isotropic turbulence with $Re_\lambda = 202$ in Watanabe & Nagata (2023). The graph reveals a decrease in the mean intensities of both motions with an increase in scale. While the maximum L_f/η value available in the DNS is smaller than the experimental range, an extrapolation of the DNS results shows alignment with the experimental data. According to Kolmogorov's second similarity hypothesis, the first moment of the filtered velocity gradient, such as the mean vorticity magnitude $\overline{|\tilde{\omega}|}$, varies as $L_f^{-2/3}$ when L_f is in the inertial subrange (Naso & Pumir 2005). Figure 7 also compares $\overline{\tilde{I}_S}$ and $\overline{\tilde{I}_R}$ with the Kolmogorov scaling of $L_f^{-2/3}$. Both $\overline{\tilde{I}_S}$ and $\overline{\tilde{I}_R}$ in the experiments conform to this power-law decay, with exponents close to that

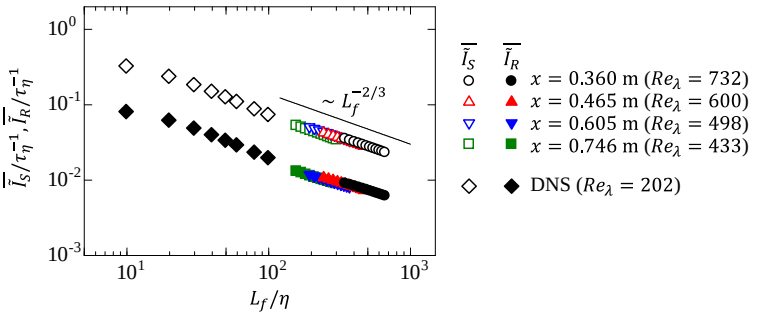

Figure 7: Scale dependence of the mean intensities of shear and rigid-body rotation, $\overline{\tilde{I}_S}$ and $\overline{\tilde{I}_R}$. The DNS results of isotropic turbulence are shown for comparison (Watanabe & Nagata 2023).

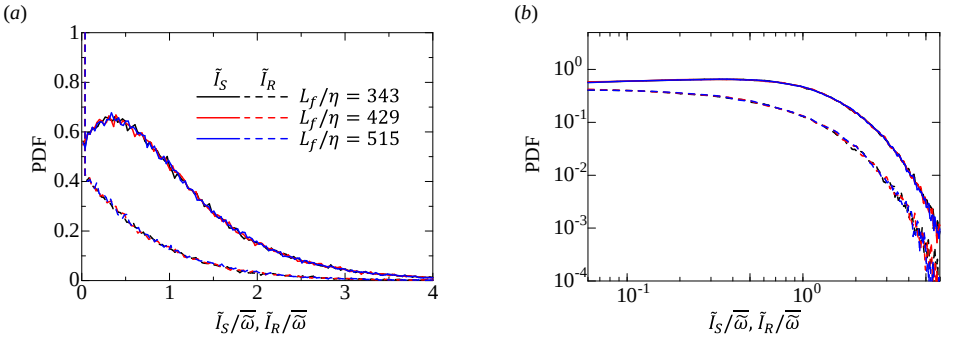

Figure 8: The probability density functions of the intensities of shear, $\tilde{I}_S$, and rigid-body rotation, $\tilde{I}_R$, of filtered velocity fields in (a) linear and (b) logarithmic scales. The results are presented for the PIV data measured at x = 0.360 m.

predicted by Kolmogorov scaling. The exact values of these exponents, determined using a least squares method, are further discussed in relation to higher-order moments below.

Figure 8 compares the probability density functions (PDFs) of $\tilde{I}_S$ and $\tilde{I}_R$ for three different values of the filter length L_f. In this comparison, the mean vorticity magnitude of the filtered velocity, $\overline{|\tilde{\omega}|}$, is utilised to normalise $\tilde{I}_S$ and $\tilde{I}_R$. The PDFs are displayed using linear and logarithmic scales in figure 8(a) and (b), respectively. The distribution of the PDFs remains consistent across different scales. The PDF of $\tilde{I}_R$ displays a pronounced peak at $\tilde{I}_R = 0$, indicating that rigid-body rotation is mostly negligible. Conversely, the PDF of $\tilde{I}_S$ peaks at $\tilde{I}_S = 0.35$, signifying the prevalence of weak shearing motion in the flow. This observation aligns with the visualisations presented in figure 6. The minimal scale-dependence of the PDFs suggests that both shear and rigid-body rotation motions are distributed within turbulence independently of scale at intermediate scales.

4.2. *Scaling of higher-order moments*

Kolmogorov's second similarity hypothesis suggests that the nth-order moment of the velocity difference between two points separated by a distance r, commonly referred to as the nth-order structure function, should follow a power law of $r^{n/3}$. Previous research has extensively demonstrated that the scaling exponents deviate from $n/3$ as n increases. This study revisits this topic, particularly focusing on shearing motion and rigid-body rotation

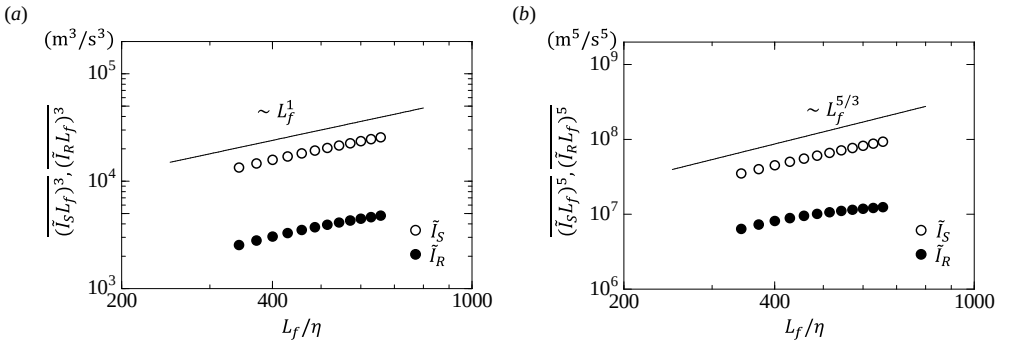

Figure 9: Scale dependence of (*a*) third- and (*b*) fifth-order moments of the velocity increments due to shear, $\tilde{I}_S L_f$, and rigid-body rotation, $\tilde{I}_R L_f$. The solid lines indicate the Kolmogorov scaling.

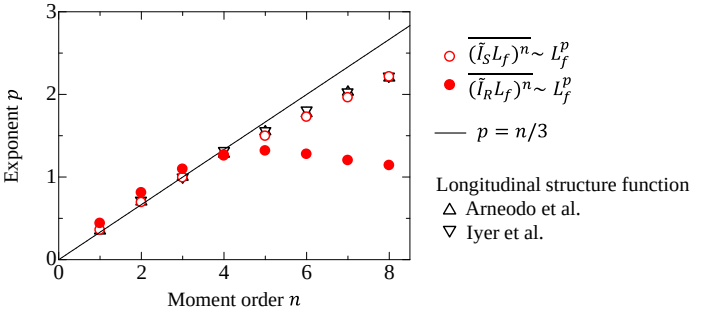

Figure 10: The power law exponents p for the nth-order moments of the velocity increments due to shear, $\tilde{I}_S L_f$, and rigid-body rotation, $\tilde{I}_R L_f$, at $x = 0.360$ m.

associated with shear layers and vortex tubes. It is important to clarify that our aim is not to establish the precise scaling exponents but rather to discuss the relevance of small-scale intermittency with these motions, which can be instrumental in understanding the statistical properties of turbulence in terms of flow structures. In the filtered velocity field with a filter length of L_f, the velocity increments due to shear and rigid-body rotation over the distance of L_f are measured as $\tilde{I}_S L_f$ and $\tilde{I}_R L_f$, respectively. The present study investigates the L_f dependence of nth-order moments of $\tilde{I}_S L_f$ and $\tilde{I}_R L_f$, denoted as $\overline{(\tilde{I}_S L_f)^n}$ and $\overline{(\tilde{I}_R L_f)^n}$. According to Kolmogorov's hypothesis, these are predicted to scale as $L_f^{n/3}$ in the inertial subrange, while smaller exponents are expected under the influence of small-scale intermittency. Figure 9 compares the results for $n = 3$ and 5 at $x = 0.360$ m with the Kolmogorov scaling. The maximum filter length considered here is $L_f/\eta = 659$, which is significantly smaller than the integral scale $L_u/\eta = 1635$. The longitudinal energy spectrum of streamwise velocity, $E_u(k_x)$, at this measurement location has been detailed in Mori *et al.* (2024). At the wavenumber corresponding to $L_f/\eta = 659\eta$, specifically $k_x\eta = 9 \times 10^{-3}$, the spectrum exhibits a clear power law of $E_u \sim k_x^{-5/3}$. This indicates that the fitting range of L_f/η falls well within the inertial subrange. For shearing motion, both $\overline{(\tilde{I}_S L_f)^3}$ and $\overline{(\tilde{I}_S L_f)^5}$ conform to power laws as a function of L_f. However, the results for rigid-body rotation tend to diverge from these power laws, particularly for $L_f/\eta > 500$.

The exponents p for the power laws $\overline{(\tilde{I}_S L_f)^n} \sim L_f^p$ and $\overline{(\tilde{I}_R L_f)^n} \sim L_f^p$ are determined using

a least squares method. For shear, the exponent associated with $\overline{(\tilde{I}_S L_f)^n}$ is evaluated across the entire range of L_f examined in the experiments. Because of the limited range of the power law for $\overline{(\tilde{I}_R L_f)^n}$, p for rigid-body rotation is calculated using data points for $L_f/\eta \leqslant 480$. In this range, the slopes of $\overline{(\tilde{I}_S L_f)^3}$ and $\overline{(\tilde{I}_R L_f)^3}$ are found to be similar, as shown in figure 9(a). Figure 10 presents the exponents p of $\overline{(\tilde{I}_S L_f)^n}$ and $\overline{(\tilde{I}_R L_f)^n}$ at $x = 0.360$ m. We have also confirmed that similar results are obtained for different measurement locations. These results are compared with the scaling exponents of the longitudinal structure function reported in Arneodo *et al.* (1996) and Iyer *et al.* (2020). For shear intensity, the exponents closely match those of the structure function: p aligns with the Kolmogorov scaling of $p = n/3$ for $n \leqslant 4$ but diverges for higher n. The extent of deviation from $p = n/3$ is quantitatively consistent between the shear intensity and the longitudinal structure function. The deviation from $p = n/3$ for $n \leqslant 4$ in rigid-body rotation is also minimal. However, the exponent p for higher-order moments of $\tilde{I}_R L_f$ is significantly smaller than $n/3$ and differs from those for $\tilde{I}_S L_f$ and the structure functions. Shearing motion is characterised by a transverse velocity gradient of $\nabla \tilde{\boldsymbol{u}}_S$ in the basic reference frame of the triple decomposition. However, in other frames, such as the laboratory coordinate $\boldsymbol{x}$, $\nabla \boldsymbol{u}_S$ can exhibit non-zero diagonal components (longitudinal velocity gradient). Therefore, comparing the exponents between shear intensity and longitudinal structure function is meaningful. While it is known that the transverse structure function for $n \geqslant 4$ has smaller scaling exponents than the longitudinal one, this discrepancy is not substantial for $n \leqslant 8$ examined here (Dhruva *et al.* 1997; Gotoh *et al.* 2002; Iyer *et al.* 2020).

The alignment of the scaling exponent between shear intensity and structure function suggests that velocity increments between two points separated by a distance r are predominantly influenced by shearing motion at the scale of r. Consistently, regions characterised by intense velocity gradients even at the smallest scale are predominantly influenced by shear (Das & Girimaji 2020). Additionally, the intensity of rigid-body rotation demonstrates scaling exponents that are considerably smaller than the Kolmogorov scaling of $n/3$. This observation aligns with the markedly intermittent distribution of rigid-body rotation, characterising vortex tubes, as visualised in figure 6(a). As discussed with conditional averages below, shearing motion at intermediate scales is concentrated in sheet-like structures, manifesting as shear layers. These results suggest that velocity increments between two points are predominantly influenced by shear layers. Iyer *et al.* (2020) explored the scaling exponents of longitudinal and transverse structure functions, noting that the exponents for high-order transverse structure functions tend to stay around 2. This behaviour and the fractal description of small-scale turbulence also suggest that sheet-like structures dominate transverse velocity increments. The present analysis further provides direct evidence supporting the relevance of shearing motion associated with layer structures to the observed deviation from the Kolmogorov scaling.

4.3. *Characteristics of shear layers at intermediate scales*

The conditional statistics evaluated near the local maxima of shear intensity are examined to investigate the flow structure associated with shearing motion at intermediate scales. The results are first presented for different filter lengths and turbulent Reynolds numbers. In § 4.4, the findings are then compared with small-scale shear layers characterised by the Kolmogorov scales.

Figure 11 provides a visualisation of the mean shear intensity $\langle \tilde{I}_S \rangle$ and mean velocity vectors in the filtered velocity fields for filter lengths $L_f/\eta = 343$ and 458. The mean velocity vectors indicate that flows in both $\pm\zeta_1$ directions, for $\zeta_2 > 0$ and $\zeta_2 < 0$, contribute to the

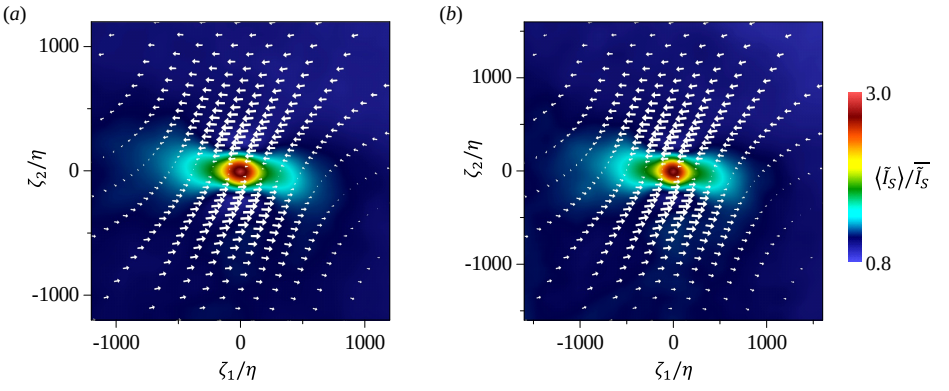

Figure 11: The mean shear intensity $\langle\tilde{I}_S\rangle$ and mean velocity vectors $(\langle\tilde{u}_1^{(s)}\rangle, \langle\tilde{u}_2^{(s)}\rangle)$ around locally intense shear regions of filtered velocity fields at filter lengths of (a) $L_f/\eta = 343$ and (b) $L_f/\eta = 458$. The vector lengths indicate the velocity magnitude. The coordinate is normalised by the Kolmogorov scale η. The results are shown for $x = 0.360$ m and $C_{th} = 2$.

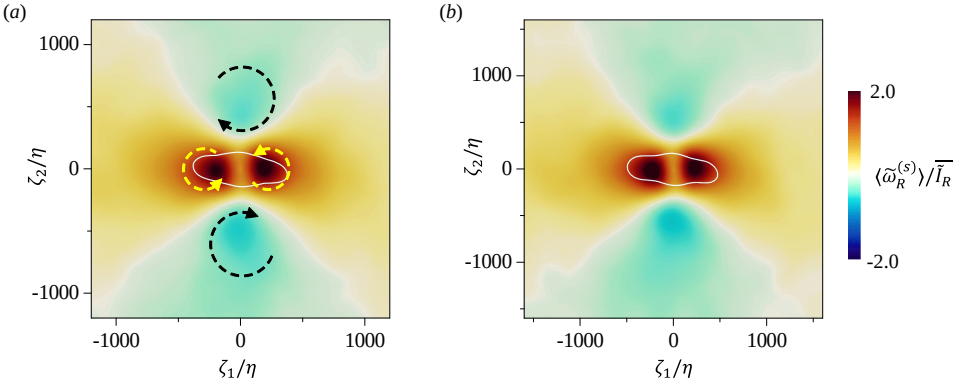

Figure 12: The distribution of mean vorticity of rigid-body rotation $\langle\tilde{\omega}_R^{(s)}\rangle$ near the shear layers at filter lengths of (a) $L_f/\eta = 343$ and (b) $L_f/\eta = 458$. The white solid line is the isoline of mean shear intensity $\langle\tilde{I}_S\rangle = 1.5\overline{\tilde{I}_S}$, indicating the shear layer location. The results are shown for $x = 0.360$ m and $C_{th} = 2$. The arrows illustrate the orientation of vortical motions.

shear. The area exhibiting large shear intensity is narrow in the ζ_2 direction but elongated along the ζ_1 axis. This observation confirms the formation of layer structures with shearing motion at intermediate scales. Notably, the mean flow pattern remains consistent across both length scales examined. The aspect ratio of the shear layer is determined by analysing the profiles of $\langle\tilde{I}_S\rangle$ along the ζ_1 and ζ_2 axes. The normalised mean shear intensity is defined as $\hat{I}_S(\zeta_1, \zeta_2) = (\langle\tilde{I}_S\rangle(\zeta_1, \zeta_2) - \overline{\tilde{I}_S})/(\langle\tilde{I}_S\rangle(0, 0) - \overline{\tilde{I}_S})$, which diminishes from 1 to 0 as $|\zeta_1|$ or $|\zeta_2|$ increases from 0. The extent of the shear layer in the ζ_1 direction, L_1, is measured as the distance between two points where $\hat{I}_S(\zeta_1, 0) = 0.1$. Likewise, the dimension of the layer in the ζ_2 direction, L_2, is determined from two points where $\hat{I}_S(0, \zeta_2) = 0.1$. The profiles of $\hat{I}_S$ have been evaluated for all measurement locations and filter lengths, confirming an aspect ratio $A_R = L_1/L_2 \approx 4.5$, which remains consistent irrespective of L_f and Re_λ.

Figure 12 displays the conditional average of the mean vorticity of rigid-body rotation,

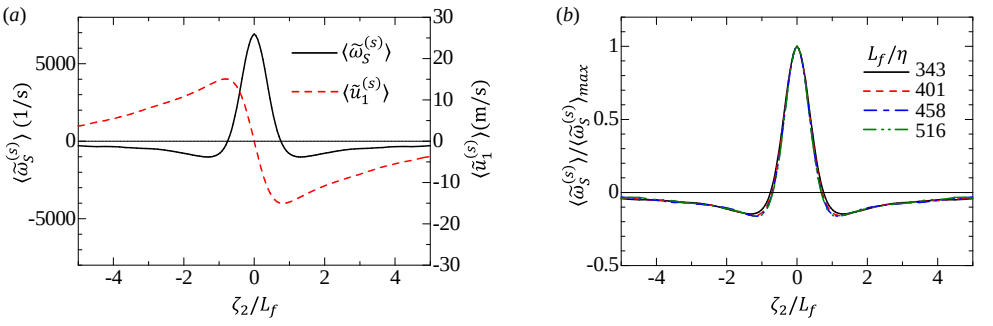

Figure 13: (a) The mean shear vorticity $\langle\tilde{\omega}_S^{(s)}\rangle$ and the mean velocity in the ζ_1 direction, $\langle\tilde{u}_1^{(s)}\rangle$, across the shear layer at $\zeta_1 = 0$ in filtered velocity fields at a filter length of $L_f/\eta = 343$. (b) The scale dependence of the mean shear vorticity normalised by the maximum value. The results are shown for $x = 0.360$ m.

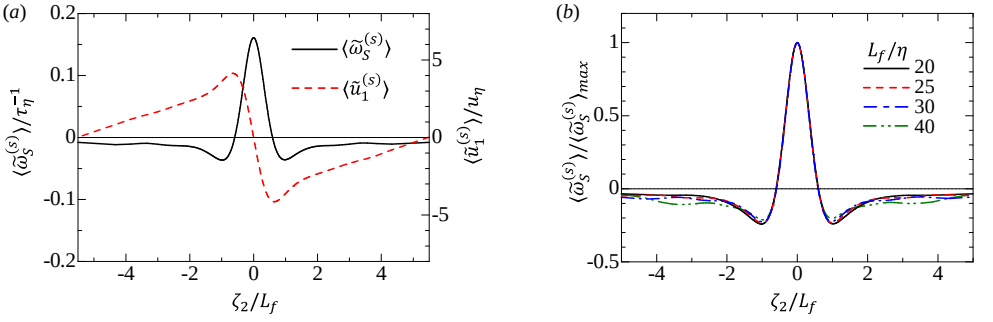

Figure 14: The same plots as in figure 13 obtained for random velocity: (a) the mean shear vorticity and mean velocity for $L_f/\eta = 30$; (b) the mean shear vorticity normalised by its peak value.

$\langle\tilde{\omega}_R^{(s)}\rangle$, in the shear coordinate. These results are obtained from the filtered velocity fields with filter lengths $L_f/\eta = 343$ and 458. The white solid line represents the location of the shear layer, marked by the isoline of the mean shear intensity. Large positive values of $\langle\tilde{\omega}_R^{(s)}\rangle$ are observed at the edges of the shear layer on $\zeta_2 = 0$. Furthermore, regions of negative $\langle\tilde{\omega}_R^{(s)}\rangle$ are present on both sides of the shear layer. This distribution pattern is the same for both filter lengths. Figure 12(a) also illustrates the orientation of the vortical motion, as determined by the sign of $\langle\tilde{\omega}_R^{(s)}\rangle$. The flow induced by rigid-body rotation is aligned with the mean flow surrounding the shear layer, as visualised in figure 11.

Figure 13(a) shows the mean shear vorticity $\langle\tilde{\omega}_S^{(s)}\rangle$ and the mean velocity in the ζ_1 direction, $\langle\tilde{u}_1^{(s)}\rangle$, across the shear layer at $\zeta_1 = 0$. The shear vorticity is significantly large within the thin layer. It approaches zero for large $|\zeta_2|$, indicating that the shearing motion identified at $\zeta_2 = 0$ weakly influence the far-field characteristics with large $|\zeta_2|$. Concurrently, the mean velocity associated with the shear, $\langle\tilde{u}_1^{(s)}\rangle$, exhibits a distinct jump within the region where $\langle\tilde{\omega}_S^{(s)}\rangle$ is large. The observed pattern of the mean velocity jump in the shear layers within the filtered velocity field aligns with the mean velocity profiles around small-scale shear layers in prior studies (Eisma *et al.* 2015; Watanabe *et al.* 2020; Fiscaletti *et al.* 2021).

The thickness δ_S and velocity jump Δu of the averaged shear layers are quantified with the half-width of $\langle\tilde{\omega}_S^{(s)}\rangle$. The definition of δ_S and Δu is chosen to directly compare with previous studies on small-scale shear layers, which employ the half-width to quantify δ_S and Δu.

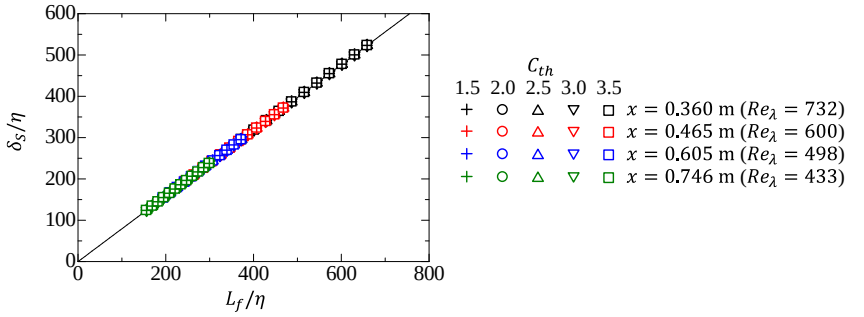

Figure 15: The scale dependence of the shear layer thickness δ_S estimated as the half-width of the mean shear vorticity. The line indicates $\delta_S = 0.79L_f$ obtained with a least squares method.

Figure 13(b) shows $\langle\tilde{\omega}_S^{(s)}\rangle$ at $\zeta_1 = 0$ normalised by its maximum value at $(\zeta_1, \zeta_2) = (0, 0)$. The distribution of the normalised shear vorticity is identical for different filter lengths, indicating the presence of self-similar structures of shearing motion at intermediate scales.

Randomly fluctuating velocity fields exhibit shearing motion, even if they are not the solutions to the Navier–Stokes equations (Watanabe *et al.* 2020). The scale dependence of shear layers is explored for a multi-scale, random and solenoidal velocity field. This velocity field possesses the same energy spectrum as homogeneous isotropic turbulence at $Re_\lambda = 128$, but with phases in wavenumber space generated by random numbers. The random velocity, free from the dynamics of Navier–Stokes equations, is frequently investigated to understand the kinematic nature of multi-scale velocity fields (Shtilman *et al.* 1993; Tsinober 2009). Details on the generation of random velocity are provided in appendix B. Figure 14 presents the conditional statistics of shear layers for the random velocity, while analogous statistics in genuine turbulence are depicted in figure 13. In figure 14(a), the shear layer within the random velocity also displays significant shear vorticity at its centre, across which the velocity changes abruptly. These profiles show little difference between turbulence and random velocity. Moreover, the shear vorticity near shear layers at different scales, as shown in figure 14(b), maintains a self-similar profile even in random velocity. These findings indicate that the self-similar layer structure with shear at intermediate scales arises primarily from the kinematic nature of multi-scale random velocities.

Figure 15 presents the relationship between the layer thickness δ_S and the filter length L_f at four measurement locations. The figure also compares results obtained using various thresholds C_{th}. As expected from the filter characteristics, δ_S linearly increases with L_f. A least squares method yields $\delta_S = 0.79L_f$. Notably, this relationship is independent of C_{th}. When analysing shear layers in the filtered velocity field, the thickness of these layers is determined by the chosen filter length.

The layer thickness δ_S is determined as the distance between the two points with $\langle\tilde{\omega}_S^{(s)}\rangle/\langle\tilde{\omega}_S^{(s)}\rangle_{max} = 0.5$, where $\langle\tilde{\omega}_S^{(s)}\rangle_{max}$ is $\langle\tilde{\omega}_S^{(s)}\rangle$ at $(\zeta_1, \zeta_2) = (0, 0)$. The mean velocity gradient caused by shear is represented by $\langle\tilde{\omega}_S^{(s)}\rangle$ at $(\zeta_1, \zeta_2) = (0, 0)$, by which the mean velocity jump across the shear layer is evaluated as $\Delta u = \delta_S\langle\tilde{\omega}_S^{(s)}\rangle$. Figure 16($a$) displays the relationship between the velocity jump of the shear layer, $\Delta u(L_f)$, and the shear layer thickness, $\delta_S(L_f)$. The Kolmogorov velocity and length scales, independent of L_f, normalise Δu and δ_S, respectively. The range of L_f, the measurement locations and the values of C_{th} are the same as in figure 15. Applying larger C_{th} values leads to the exclusion of weaker shearing motions from the analysis, which consequently results in an increase in Δu as C_{th}

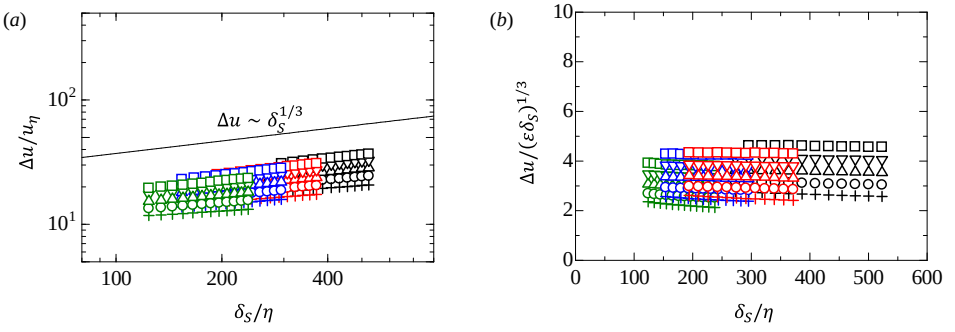

Figure 16: (*a*) The scale dependence of the mean velocity jump Δu across the shear layer. (*b*) The compensated plots of Δu normalised by $(\varepsilon\delta_S)^{1/3}$. Symbols are the same as in figure 15.

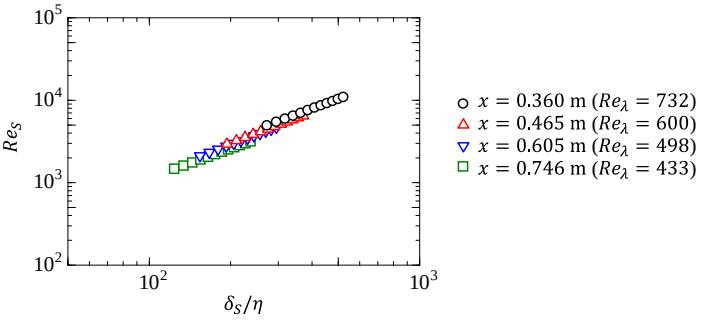

Figure 17: The scale dependence of the shear Reynolds number. The results are presented for $C_{th} = 1.5$.

increases. Despite this increase, the scale dependence of Δu remains similar for all C_{th} values, showing that Δu increases with δ_S. According to the Kolmogorov scaling, the velocity jump across a shear layer of thickness δ_S is predicted to scale as $\Delta u \sim (\varepsilon\delta_S)^{1/3}$. The slope of Δu closely follows this power law. This power law is more evident in the compensated plot shown in figure 16(*b*), where $\Delta u/(\varepsilon\delta_S)^{1/3}$ is plotted against δ_S/η. The scale-dependence of $\Delta u/(\varepsilon\delta_S)^{1/3}$ is insignificant, suggesting that $\Delta u \sim (\varepsilon\delta_S)^{1/3}$ is generally valid for the present data. However, the results also indicate that the coefficient A in $\Delta u = A(\varepsilon\delta_S)^{1/3}$ is not universal but varies with C_{th}. This variation is attributed to the elimination of weaker shearing motions at higher C_{th} values. For $C_{th} = 1.5$, the value of A is approximately between 2.5 ± 0.2 for $Re_\lambda = 433$–732. The velocity jump Δu evaluated on two-dimensional planes is underestimated by a factor of about $1/\sqrt{3}$ compared to that in three-dimensional fields, as demonstrated in appendix A. Consequently, the actual velocity jump is more accurately expressed as $\Delta u = A'(\varepsilon\delta_S)^{1/3}$, where $A' \approx \sqrt{3}A \approx 4.3$.

Figure 17 illustrates the scale dependence of the shear Reynolds number, Re_S, a crucial parameter characterising the dynamics of shear layers. The shear Reynolds number is defined using the thickness and velocity jump of the shear layer as $Re_S = \delta_S\Delta u/\nu$. Given the Kolmogorov scaling for the velocity jump, $\Delta u \sim \delta_S^{1/3}$, Re_S is expected to obey a power law of δ_S written as $Re_S \sim \delta_S^{4/3}$. Consistently, $Re_S \sim (\delta_S/\eta)^{1.3}$ is obtained with a least squares method. The shear Reynolds number is also underestimated by the two-dimensional analysis of three-dimensional shearing motions, as discussed in appendix A. The actual shear

Reynolds number is about $\sqrt{3}$ times larger than the values presented in figure 17. The shear Reynolds number in the intermediate scales is sufficiently large for the shear layers to be unstable. This point is further discussed in § 4.4.

4.4. *Comparisons of shear layers at intermediate scales and the smallest scale*

The findings from this study on shear layers at intermediate scales show similarities to the characteristics of small-scale shear layers previously investigated. The latter has been investigated with the triple decomposition of the fully-resolved velocity gradient tensor (Eisma *et al.* 2015; Hayashi *et al.* 2021*a*; Fiscaletti *et al.* 2021; Watanabe & Nagata 2022, 2023). Here, these shear layers are compared between the intermediate scales and the smallest scale.

The mean profile of shear intensity depicted in figure 11 reveals that the aspect ratio, A_R, of the shear layer in the mean flow pattern is approximately 4.5. This same methodology for assessing the aspect ratio is applicable to the mean shear intensity profile of the small-scale shear layer presented in previous studies. For instance, in a turbulent planar jet with $Re_\lambda = 97$ in Hayashi *et al.* (2021*a*), the small-scale shear layer has $A_R = 4.6$, which aligns closely with $A_R = 4.5$ observed for the shear layers at intermediate scales. Moreover, the two-dimensional distribution of the mean shear intensity and mean velocity vector, as shown in figure 11, resembles the distribution pattern found for small-scale shear layers (Hayashi *et al.* 2021*a*).

Figure 12 indicates the presence of vortex tubes exhibiting rigid-body rotation near the shear layers at intermediate scales. The sign of the rigid-body rotation vorticity, $\tilde{\omega}_R^{(s)}$, reveals that the vortices within the shear layer (where $\tilde{\omega}_R^{(s)} > 0$) rotate in the same direction as the shear-induced vorticity ($\tilde{\omega}_S^{(s)} > 0$). Conversely, vortices located alongside the shear layers exhibit the opposite sign of $\tilde{\omega}_R^{(s)}$. Watanabe & Nagata (2022) presented similar observations for small-scale shear layers, where pairs of anti-rotating vortices associated with rigid-body rotation were also noted in the mean profile around the shear layers. Thus, the arrangement of vortices around shear layers appears consistent across both intermediate and small scales. In the case of small-scale shear layers, it is understood that the vortices on the sides of the shear layer contribute to the flow that drives the shearing motion (Watanabe & Nagata 2022). This role of vortices is likely comparable at the intermediate scale because of the similar configurations of vortices. These findings suggest that shear layers often emerge adjacent to rotating motion, aligning with earlier research on tubular and sheet-like structures at intermediate scales (Bermejo-Moreno *et al.* 2009). These structures tend to appear next to each other. However, given that rigid-body rotation is more spatially intermittent than shearing motion, such vortex configurations may not be present for all shear layers in instantaneous flow fields.

Watanabe & Nagata (2023) investigated the shear Reynolds number, Re_S, for small-scale shear layers in homogeneous isotropic turbulence, defined using the half-width of the shear intensity, δ_S, and the velocity jump, Δu, across the layers. The characteristics of small-scale shear layers are compared with the scale dependence of Δu and Re_S at intermediate scales (greater than 100η) derived from the current experimental data. Figure 16 demonstrates the Kolmogorov scaling for the velocity jump, $\Delta u = A'(\varepsilon\delta_S)^{1/3}$, with $A' \approx 4.3$ for the smallest C_{th}. This lowest threshold value is selected to include even weak shearing motions, akin to the analyses of small-scale shear layers in Watanabe & Nagata (2023). The present results for Δu yield the following relationship for the mean velocity jump of shear layers in the inertial subrange:

$$\Delta u/u_\eta = A'(\delta_S/\eta)^{1/3}. \tag{4.1}$$

The time scale associated with the evolution of shear layers is defined as $\tau_S = \delta_S/\Delta u$. The small-scale shear layers often collapse, forming small-scale vortex tubes through shear instability, as described in Vincent & Meneguzzi (1994). The time scale of this shear instability is comparable to τ_S and is of the same order as the Kolmogorov time scale τ_η for the small-scale shear layers (Watanabe & Nagata 2023). Equation (4.1) yields the following expression for τ_S:

$$\tau_S/\tau_\eta = A'^{-1}(\delta_S/\eta)^{2/3}, \tag{4.2}$$

which can be related to the time period for vortex formation from shear layers at scale δ_S. Finally, (4.1) yields the shear Reynolds number as follows:

$$Re_S = A'(\delta_S/\eta)^{4/3}. \tag{4.3}$$

These relationships are based on the Kolmogorov scaling of the velocity jump Δu within the inertial subrange. However, they align well with the characteristics of small-scale shear layers. Typically, these small-scale shear layers were shown to have $\delta_S \approx 4\eta$, $\Delta_u \approx 5u_\eta$ and therefore $Re_S = (\delta_S/\eta)(\Delta_u/u_\eta) \approx 20$ (Watanabe & Nagata 2023). Equation (4.1) specifically predicts $\Delta u = 6.8u_\eta$ for a shear layer thickness of $\delta_S = 4\eta$, closely matching the direct observation of $\Delta u \approx 5u_\eta$ for the small-scale shear layers. This congruence suggests that other characteristics of small-scale shear layers are also consistent with the estimations based on the Kolmogorov scaling. For instance, (4.2) with $\delta_S = 4\eta$ predicts $\tau_S = 0.6\tau_\eta$, aligning with $\tau_S = 0.8\tau_\eta$, which is directly evaluated for small-scale shear layers. Additionally, (4.3) with $\delta_S \approx 4\eta$ yields $Re_S = 27$, closely resembling the reported value of $Re_S = 20$ for small-scale shear layers. Despite the strong influence of viscosity on small-scale shear layers, as evidenced by the kinetic energy and enstrophy budgets (Pirozzoli *et al.* 2010; Hayashi *et al.* 2021*a*; Watanabe & Nagata 2022), the empirical relations rooted in Kolmogorov scaling are surprisingly consistent with the small-scale shear layers. This implies that (4.1–4.3) are applicable even to the shear layers at smaller scales than examined in this study.

The shear layers at intermediate scales exhibit a high shear Reynolds number ($Re_S \gg 1$), indicating their instability against perturbations (Betchov & Szewczyk 1963; Lin & Corcos 1984). The mean shear intensity profile displayed in figure 11 reveals an aspect ratio of approximately 4.5 for these layers. Such a low aspect ratio suggests that the shear layers are absolutely unstable, even in the absence of external perturbations. This is due to the self-induced velocity of the shear layers, which initiates the self-roll-up process of the layers (Watanabe & Nagata 2023). The present results imply that the instability of shear layers with thickness δ_S within the inertial subrange readily leads to the formation of vortex tubes of a similar scale. Theoretical and numerical analyses of shear instability have confirmed that the shear layer possesses an optimal wavelength for disturbances, which most effectively accelerates the roll-up of the shear layers (Betchov & Szewczyk 1963; Lin & Corcos 1984). For shear layers with a finite aspect ratio, this optimal wavelength is around 7 times the thickness defined as the half-width of the shear intensity (Watanabe & Nagata 2023). Both perturbation-induced and self-induced instabilities of shear layers with a finite aspect ratio are further accelerated by external disturbances with a length scale of $7\delta_S$. Small-scale shear layers with $\delta_S \approx 4\eta$ in isotropic turbulence are indeed particularly unstable against perturbations at this wavelength, which corresponds to about 28η (Watanabe & Nagata 2023). This scale dependence in the response of shear layers to perturbations can be important in understanding the interaction of turbulent motions with different scales in terms of flow structures. Additionally, the instability of shear layers within the inertial range can also be crucial in understanding the modulation of turbulence by disturbances, such as flows interacting with cylinders, spheres, or particles (Nagata *et al.* 2020*b*; Takamure *et al.* 2023), when the disturbance scale matches the instability mode of shear layers at a specific scale. This

aspect will also be important in studies of flow control, which often leverage flow instability to maximize the impact of disturbances introduced into flows (Cattafesta III & Sheplak 2011; Watanabe 2024).

5. Conclusion

The scale dependence of local shearing motion has been explored through wind tunnel experiments of decaying homogeneous isotropic turbulence generated by multiple jets, with the turbulent Reynolds number ranging approximately from 900 to 400. The PIV datasets in Mori *et al.* (2024) were analysed using the triple decomposition (Kolář 2007) applied to filtered velocity fields. This decomposition separates the coarse-grained velocity gradient tensor into three components: shear, rigid-body rotation and elongation, each associated with a specific scale determined by the filter cutoff L_f. Vortex tubes and shear layers (also called vortex sheets) are linked to rigid-body rotation and shear. Here, L_f falls within intermediate scales, specifically greater than 100η, and is expected to lie in the inertial subrange.

The analysis of the instantaneous distribution of rigid-body rotation and shear, along with the PDFs of their intensities, $\tilde{I}_S$ and $\tilde{I}_R$, at the scale of L_f reveals that rigid-body rotation exhibits more spatial intermittency compared to shearing motion. Shearing motion is present almost everywhere in turbulence, whereas most flow regions exhibit negligible rigid-body rotation. As the scale L_f increases, the mean intensities of rigid-body rotation and shear decrease, following power laws with exponents close to the Kolmogorov scaling of $L_f^{-1/3}$ for the inertial subrange. Additionally, the moments of velocity increments caused by shear and rigid-body rotation, defined through their intensities as $\tilde{I}_S L_f$ and $\tilde{I}_R L_f$, are investigated across various scales. The moments of the velocity increment due to shear, $\overline{(\tilde{I}_S L_f)^n}$, obey power laws of L_f, denoted as $\overline{(\tilde{I}_S L_f)^n} \sim L_f^p$. This analysis reveals anomalous scaling for the shear intensity, where the exponent $p(n)$ is smaller than the Kolmogorov scaling of $p = n/3$ for larger values of n. This deviation from the Kolmogorov scaling aligns quantitatively with that observed for the longitudinal structure function, suggesting that the velocity increment between two points is predominantly influenced by shearing motion with the scale of two-point distance. The moments of the velocity increment attributable to rigid-body rotation, $\overline{(\tilde{I}_R L_f)^n}$, also follow power laws, albeit over a narrower range compared to shear. The exponent for $\overline{(\tilde{I}_R L_f)^n} \sim L_f^p$ deviates more significantly from $n/3$ than that of shear. This larger deviation is consistent with the more intermittent distributions of rigid-body rotation observed in the flow.

The mean flow structure associated with shearing motion was further explored through conditional averages around regions with locally intense shear. In these analyses, the shear layer manifests between parallel mean flows in opposite directions. The observed shear layer exhibits an aspect ratio of approximately 4.5 and is found in proximity to rotational motions, characteristic of vortex tubes. The aspect ratio of the shear layer and the configuration of these vortices at intermediate scales align with those of small-scale shear layers at the Kolmogorov scale. The mean shear layer pattern remains consistent when scaled with the filter length, suggesting self-similar structures of shearing motion across different scales. A comparison between turbulence and random velocity has indicated that the self-similar shear layers at different scales arise from the kinematic nature of multi-scale velocity fluctuations. The mean velocity jump Δu across the shear layer increases with the layer thickness δ_S. This increase aligns well with the Kolmogorov scaling, as denoted in (4.1), leading to similar power laws for the time scale and Reynolds number of shear layers, as given in (4.2) and (4.3). Although

these power laws are based on the Kolmogorov scaling within the inertial subrange, their extension to smaller scales effectively predicts the characteristics of small-scale shear layers.

The scaling exponents of shear intensity underscore the significance of shearing motion at intermediate scales, which may surpass rigid-body rotation in influencing some scale-dependent turbulence properties. These motions are manifested as vortex tubes and shear layers. Numerous efforts have been made to model turbulence by conceptualising it as being composed of spatially distributed simple structures (Townsend 1976; Lundgren 1993; Marusic & Monty 2019). Notably, a simple model of small-scale shear layers, based on the mean flow pattern directly observed for small-scale shearing motion within turbulent flows, has successfully elucidated the response of turbulence to small-scale perturbations (Watanabe & Nagata 2023). The self-similarity observed in the shear layers offers an advantage in constructing models of these layers at various scales. The mean flow structure of shearing motion and its scaling properties, revealed in this study, hold the potential for enhancing our understanding of turbulent flows in the context of flow structures.

Acknowledgements. Numerical simulations presented in this paper were performed using the high-performance computing systems at the Japan Agency for Marine-Earth Science and Technology and Nagoya University. This work was also supported by Collaborative Research Project on Computer Science with High-Performance Computing in Nagoya University.

Funding. This work was supported by JSPS KAKENHI Grant Nos. 22K03903 and 22H01398.

Declaration of interests. The authors report no conflict of interest.

Data availability statement. The data that support the findings of this study are available from the corresponding author upon reasonable request.

Appendix A. Comparison of the triple decomposition between two- and three-dimensional velocity gradient tensors

The present study has analysed the two-dimensional velocity gradient measured by PIV. The triple decomposition is used to extract three motions from two-dimensional planes even though turbulence involves three-dimensional fluid motions. This appendix investigates the discrepancies in the triple decomposition between two-dimensional (2D) and three-dimensional (3D) velocity gradient tensors using the DNS database of homogeneous isotropic turbulence, the same database previously utilised in Watanabe *et al.* (2020) and Watanabe & Nagata (2023). The DNS was conducted using an in-house finite difference code, which applies a fourth-order fully-conservative finite difference scheme and a third-order Runge–Kutta method (Morinishi *et al.* 1998). The statistically steady state was achieved through a linear forcing scheme (Carroll & Blanquart 2013). The turbulent Reynolds number is $Re_\lambda = 202$, and the simulation uses 2048^3 grid points.

The triple decomposition is applied to the low-pass filtered 3D velocity gradient tensor $(\nabla\tilde{\boldsymbol{u}})_{ij}$, where $i, j = 1, 2$ and 3, resulting in $\nabla\tilde{\boldsymbol{u}}_S$, $\nabla\tilde{\boldsymbol{u}}_R$ and $\nabla\tilde{\boldsymbol{u}}_E$. A 3D Gaussian filter with a filter length L_f is employed in wavenumber space, as described by Pope (2000). The algorithm for triple decomposition follows Nagata *et al.* (2020*a*). Similarly, the triple decomposition of the 2D filtered velocity gradient tensor described in § 3.2 is applied to the same DNS database. Both analyses provide flow statistics as functions of the filter length L_f.

Figure 18 visualises two-dimensional distributions of $\tilde{I}_R$ and $\tilde{I}_S$ derived from the 3D triple decomposition. A highly intermittent distribution of $\tilde{I}_R$ is observed, with values close to zero across most of the flow, while shear dominates a significant portion of the flow. This predominance of shear over rigid-body rotation aligns with findings from the triple decomposition of fully-resolved velocity gradient tensors (Nagata *et al.* 2020*a*;

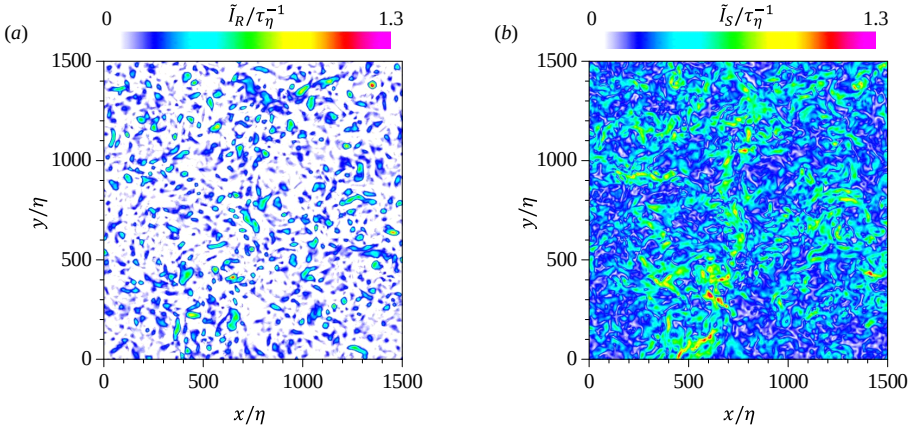

Figure 18: Two-dimensional distributions of the intensities of (a) rigid-body rotation and (b) shear evaluated using the 3D triple decomposition for a filter length of $L_f/\eta = 30$ in DNS.

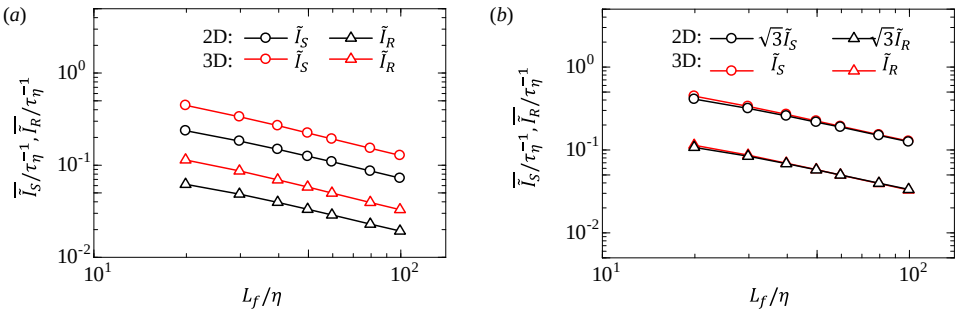

Figure 19: (a) The scale dependence of the mean intensities of shear and rigid-body rotation, $\overline{\tilde{I}_S}$ and $\overline{\tilde{I}_R}$, evaluated using 2D and 3D triple decompositions applied to DNS data of homogeneous isotropic turbulence. (b) $\overline{\tilde{I}_S}$ and $\overline{\tilde{I}_R}$ multiplied by $\sqrt{3}$ in the 2D case to account for the underestimation due to dimensionality reduction.

Das & Girimaji 2020; Hayashi *et al.* 2021a). Additionally, this tendency is also evident in the triple decomposition applied to 2D planes, as shown in figure 6.

Figure 19(a) compares the 2D and 3D triple decompositions regarding the L_f dependence of the mean intensities of shear and rigid-body rotation, $\overline{\tilde{I}_S}$ and $\overline{\tilde{I}_R}$. Both decompositions yield a similar trend: $\overline{\tilde{I}_S}$ and $\overline{\tilde{I}_R}$ decrease with L_f at a comparable rate. The mean intensities for the 2D decomposition are smaller than those for the 3D case. This discrepancy arises because the 2D decomposition only considers motions defined on an examined plane. The shear component of the velocity gradient tensor for the 2D case can be expressed in a basic reference frame as follows:

$$\nabla\tilde{\boldsymbol{u}}_S = \begin{pmatrix} 0 & a \\ 0 & 0 \end{pmatrix}. \tag{A 1}$$

For the 3D case, $\nabla\tilde{\boldsymbol{u}}_S$ in a basic reference frame is written as:

$$\nabla\tilde{\boldsymbol{u}}_S = \begin{pmatrix} 0 & a & b \\ 0 & 0 & c \\ 0 & 0 & 0 \end{pmatrix}. \tag{A 2}$$

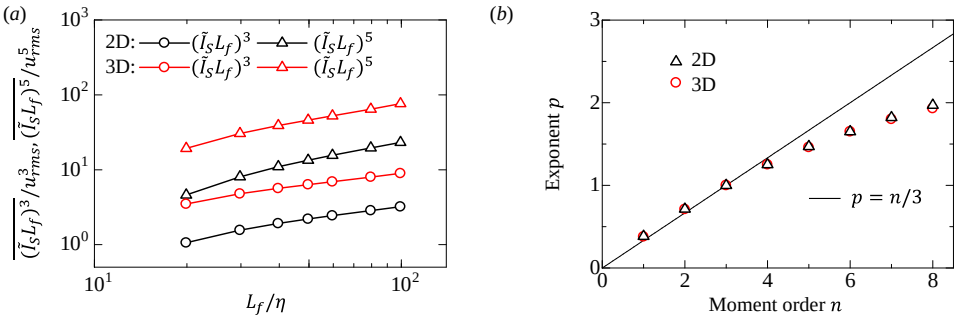

Figure 20: (a) The scale dependence of the third- and fifth-order moments of the velocity increments due to shear, $\tilde{I}_S L_f$, evaluated using 2D and 3D triple decompositions applied to DNS data. (b) The power law exponents p for the nth-order moments of $\tilde{I}_S L_f$. These exponents are evaluated using the ESS method.

It should be noted that other forms are possible as long as $\nabla \tilde{\boldsymbol{u}}_S$ remains purely asymmetric (Kolář & Šístek 2014). The shear intensity is $\tilde{I}_S = \sqrt{2}a$ for the 2D case and $\tilde{I}_S = \sqrt{2(a^2 + b^2 + c^2)}$ for the 3D case, suggesting that the shear intensity is inherently smaller on a 2D plane, which does not account for two of the three non-zero components. This explanation also holds true for the intensity of rigid-body rotation. As all non-zero components in $\nabla \tilde{\boldsymbol{u}}_S$ are statistically identical in isotropic turbulence, it can be expected that the average of $\tilde{I}_S$ in the 3D decomposition is about $\sqrt{3}$ times larger than that in the 2D case. Here, $\sqrt{3}$ for the mean intensities is not the exact value derived theoretically. Figure 19(b) presents the compensated plots, where $\tilde{I}_S$ and $\tilde{I}_R$ for the 2D case are multiplied by $\sqrt{3}$. The compensated intensities align with their 3D counterparts. Thus, the discrepancy between the 2D and 3D decompositions in figure 19(a) is attributed to the out-of-plane components of the velocity gradient tensor. Despite the difference by a factor of $\sqrt{3}$, the L_f dependence remains consistent for both 2D and 3D decompositions. Therefore, evaluating the scale dependence of shear and rigid-body rotation on 2D planes still provides valuable insights into local turbulent motions considered in the triple decomposition.

Figure 20(a) presents the third- and fifth-order moments of the velocity increments due to shear, $\tilde{I}_S L_f$, evaluated using the 2D and 3D triple decompositions. Similar to the mean shear intensity, the 2D decomposition underestimates the higher-order moments of $\tilde{I}_S L_f$. However, the L_f dependence is consistent between the 2D and 3D decompositions, suggesting that the scaling exponents in $\overline{(\tilde{I}_S L_f)^n} \sim L_f^{p(n)}$ are also similar for both cases. A direct evaluation of p using a least squares method on the plots of $\overline{(\tilde{I}_S L_f)^n}$ is unsuitable because the Reynolds number is not sufficiently high in the DNS. The scaling exponents of structure functions at moderate Reynolds numbers are often estimated with the extended self-similarity (ESS) method (Benzi *et al.* 1993; Saw *et al.* 2018; Matsushima *et al.* 2021), which determines the scaling exponents for $n \neq 3$ by plotting the nth-order structure functions against the third-order structure function. This study applies the ESS method to the nth-order moments of $\tilde{I}_S L_f$ to determine the scaling exponents. Although previous studies have shown that scaling exponents estimated with ESS align with those directly measured in experiments, it has also been argued that the ESS method can yield inaccurate estimations due to low-Reynolds number effects on the third-order structure function (Tang *et al.* 2017). Here, the ESS method is utilised solely to compare the scaling exponents of $\overline{(\tilde{I}_S L_f)^n}$ between the 2D and 3D triple decompositions and is not intended to provide exact values for the exponents. In addition,

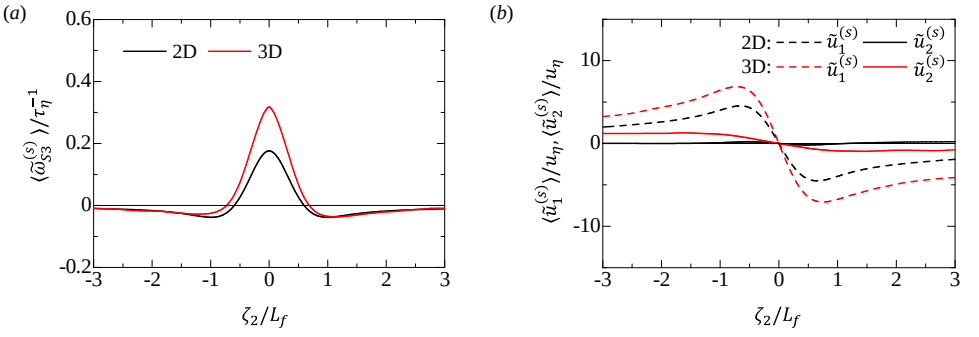

Figure 21: Conditional statistics of shear layers obtained using 2D and 3D triple decompositions in DNS of isotropic turbulence: (a) mean shear vorticity and (b) mean velocity at $L_f/\eta = 60$. Indices 1 and 2 of vectors denote the parallel and normal directions to the shear layers, respectively, while 3 represents the direction of shear vorticity at the centre of the shear layers.

the discussion is limited to shearing motion here because power laws are not observed for high-order moments of $\tilde{I}_R L_f$ with the ESS method for both the 2D and 3D cases. Figure 20(b) displays the scaling exponents of $\overline{(\tilde{I}_S L_f)^n} \sim L_f^{p(n)}$, estimated using the ESS method. The exponents are evaluated for $20 \leqslant L_f/\eta \leqslant 100$. Both the 2D and 3D decompositions yield identical scaling exponents, indicating that they are unlikely to be affected by out-of-plane motions not captured on 2D planes. These exponents are also consistent with those observed in the current experiments and those derived from longitudinal structure functions, as shown in figure 10.

The conditional statistics of shear layers are compared between the 2D and 3D triple decompositions. In both cases, the centre of shear layers is identified as a local maximum of $\tilde{I}_S$ where $\tilde{I}_S \geqslant 2\overline{\tilde{I}_S}$. For the 3D analysis, the shear coordinate $(\zeta_1, \zeta_2, \zeta_3)$ is defined using the methodology described in Hayashi *et al.* (2021a). The filtered velocity vector in the shear coordinate is represented as $(\tilde{u}_1^{(s)}, \tilde{u}_2^{(s)}, \tilde{u}_3^{(s)})$. Here, the direction of ζ_3 aligns with the direction of the shear vorticity vector $\tilde{\omega}_{Si} = \epsilon_{ijk}(\nabla\tilde{\boldsymbol{u}}_S)_{jk}$ and is given by $\tilde{\boldsymbol{\omega}}_S/|\tilde{\boldsymbol{\omega}}_S|$. The orthogonal directions ζ_1 and ζ_2 are determined such that shear is represented by $\partial\tilde{u}_1^{(s)}/\partial\zeta_2$. Details of the numerical algorithm for determining the shear coordinate are available in Hayashi *et al.* (2021a). Flow variables defined at computational grid points in DNS are interpolated onto the shear coordinate system. The discretisation and interpolation methods used are consistent with those described in § 3.3. The analysis with the 2D triple decomposition, as outlined in § 3.3, is also conducted using DNS data for comparison. The filter length L_f is set at $L_f/\eta = 60$, although the following discussion remains valid regardless of the chosen L_f.

Figure 21(a) compares the mean shear vorticity in the ζ_3 direction, $\langle\tilde{\omega}_{S3}^{(s)}\rangle$, plotted against ζ_2 across the centre of the shear layer at $(\zeta_1, \zeta_3) = (0, 0)$. The corresponding plots obtained from the experiments are presented in figure 13(a). Both 2D and 3D decompositions effectively capture the prominent peak in shear vorticity within the shear layers. The layer thickness, estimated by the mean shear vorticity, is similar for both decompositions. However, consistent with observations for the mean shear intensity in figure 19, the mean shear vorticity within the shear layer is underestimated by the 2D triple decomposition. The peak value of $\langle\tilde{\omega}_{S3}^{(s)}\rangle$ in the 3D case is $0.32\tau_\eta^{-1}$, approximately $\sqrt{3}$ times greater than that in the 2D decomposition, which is $0.18\tau_\eta^{-1}$. This indicates that the effect of evaluating shear in 2D planes is consistent across both conditional and unconditional averages.

Figure 21(b) compares the conditional average of velocity components in the ζ_1 and ζ_2 directions. The experimental results are also presented in figure 13(a). Due to the presence of shear, $\tilde{u}_1^{(s)}$ displays a velocity jump within the shear layer. The mean velocity jump, evaluated using the mean layer thickness as defined in § 4.3, is $13.2u_\eta$ in the 3D decomposition, approximately $\sqrt{3}$ times larger than $7.1u_\eta$ observed in the 2D case. This discrepancy indicates that analyses conducted on 2D planes underestimate the mean velocity jump by a factor of about $\sqrt{3}$. While the mean velocity in the layer parallel direction, $\langle\tilde{u}_1^{(s)}\rangle$, is similar for both 2D and 3D decompositions, a qualitative difference is observed in the velocity in the layer normal direction, $\tilde{u}_2^{(s)}$. In the 3D decomposition, $\langle\tilde{u}_2^{(s)}\rangle$ displays positive and negative values around $\zeta_2 = 0$. This profile suggests that the shear layer experiences compression, indicated by $\partial\tilde{u}_2^{(s)}/\partial\zeta_2 < 0$. This compression is also characteristic of small-scale shear layers and is related to an expanding flow in the direction of shear vorticity, contributing to vortex stretching (Watanabe *et al.* 2020). The presence of straining flows with both compression and expansion highlights a three-dimensional feature of shear layers. Consequently, the 2D triple decomposition fails to capture this compressive flow in the ζ_2 direction, as evidenced by $\langle\tilde{u}_2^{(s)}\rangle \approx 0$.

Appendix B. Generation of multi-scale, random and solenoidal velocity

This appendix details the generation of random velocity fields used in the comparative analysis with genuine turbulence to investigate the kinematic aspects of shear layers. The procedure follows the method described by Johnsen *et al.* (2010): velocity vectors in the physical domain, $\boldsymbol{u} = (u, v, w)$, are generated by applying the inverse Fourier transform to their counterparts in the wavenumber domain, $\hat{\boldsymbol{u}} = (\hat{u}, \hat{v}, \hat{w})$. These solenoidal velocity vectors $(\hat{u}, \hat{v}, \hat{w})$ possess a predefined three-dimensional energy spectrum $E(k)$ and random phase components. The formula for the velocity vector components is:

$$\hat{\boldsymbol{u}}(k_x, k_y, k_z) = \left(\frac{k_y}{k_{xy}}a + \frac{k_x k_z}{k_{xy}k}b,\ \ \frac{k_y k_z}{k_{xy}k}b - \frac{k_x}{k_{xy}}a,\ \ -\frac{k_{xy}}{k}b\right), \tag{B 1}$$

with

$$a = \sqrt{\frac{2E(k)}{4\pi k^2}}e^{i\phi_x}\cos(\phi_z),\ \ b = \sqrt{\frac{2E(k)}{4\pi k^2}}e^{i\phi_y}\cos(\phi_z), \tag{B 2}$$

In this expression, $\phi_\alpha(k_x, k_y, k_z)$ ($\alpha = x, y$ or z) is a random phase between 0 and 2π. The wavenumber vector is (k_x, k_y, k_z), with $k_{xy} = \sqrt{k_x^2 + k_y^2}$ and $k = \sqrt{k_x^2 + k_y^2 + k_z^2}$. After specifying $E(k)$ based on a model spectrum or DNS of turbulence, the components $(\hat{u}, \hat{v}, \hat{w})$ are calculated using (B 1) by assigning random values to ϕ_x, ϕ_y and ϕ_z. Performing the inverse Fourier transform of these components yields a random solenoidal velocity field consistent with the chosen energy spectrum. In this study, $E(k)$ is derived from the DNS database of forced homogeneous isotropic turbulence at $Re_\lambda = 128$, as detailed in Watanabe *et al.* (2020).

The present study examines 10 random velocity fields, each generated using distinct sets of random numbers for the phase assignments. These random velocity fields are discretised using 1024^3 grid points, identical to the grid resolution in the original DNS where the energy spectrum was determined. Ensemble averages across these random velocity fields result in a turbulent Reynolds number, $Re_\lambda = 128$. Visualisations of shear and rigid-body rotation at the smallest scale in these random velocity fields were presented in Watanabe & Nagata (2022).

REFERENCES

Akao, T., Watanabe, T. & Nagata, K. 2022 Vertical confinement effects on a fully developed turbulent shear layer. *Phys. Fluids* **34** (5), 055129.

Arneodo, A., Baudet, C., Belin, F., Benzi, R., Castaing, B., Chabaud, B., Chavarria, R., Ciliberto, S., Camussi, R., Chilla, F. & others 1996 Structure functions in turbulence, in various flow configurations, at Reynolds number between 30 and 5000, using extended self-similarity. *Europhys. Lett.* **34** (6), 411.

Bailey, S. C. C., Hultmark, M., Monty, J. P., Alfredsson, P. H., Chong, M. S., Duncan, R. D., Fransson, J. HM, Hutchins, N., Marusic, I., McKeon, B. J., Nagib, H. M., Örlü, R., Segalini, A., Smits, A. J. & Vinuesa, R. 2013 Obtaining accurate mean velocity measurements in high Reynolds number turbulent boundary layers using Pitot tubes. *J. Fluid Mech.* **715**, 642–670.

Benzi, R., Ciliberto, S., Tripiccione, R., Baudet, C., Massaioli, F. & Succi, S. 1993 Extended self-similarity in turbulent flows. *Phys. Rev. E* **48** (1), R29.

Bermejo-Moreno, I., Pullin, D. I. & Horiuti, K. 2009 Geometry of enstrophy and dissipation, grid resolution effects and proximity issues in turbulence. *J. Fluid Mech.* **620**, 121–166.

Betchov, R. & Szewczyk, A. 1963 Stability of a shear layer between parallel streams. *Phys. Fluids* **6** (10), 1391–1396.

Buaria, D. & Sreenivasan, K. R. 2023 Saturation and multifractality of Lagrangian and Eulerian scaling exponents in three-dimensional turbulence. *Phys. Rev. Lett.* **131** (20), 204001.

Carroll, P. L. & Blanquart, G. 2013 A proposed modification to Lundgren's physical space velocity forcing method for isotropic turbulence. *Phys. Fluids* **25** (10), 105114.

Castaing, B., Gagne, Y. & Hopfinger, E. J. 1990 Velocity probability density functions of high Reynolds number turbulence. *Phys. D* **46** (2), 177–200.

Cattafesta III, L. N. & Sheplak, M. 2011 Actuators for active flow control. *Annu. Rev. Fluid Mech.* **43**, 247–272.

Clemens, N. T. & Mungal, M. G. 1991 A planar Mie scattering technique for visualizing supersonic mixing flows. *Exp. Fluids* **11** (2-3), 175–185.

Coriton, B., Steinberg, A. M. & Frank, J. H. 2014 High-speed tomographic PIV and OH PLIF measurements in turbulent reactive flows. *Exp. Fluids* **55**, 1–20.

Das, R. & Girimaji, S. S. 2020 Revisiting turbulence small-scale behavior using velocity gradient triple decomposition. *New J. Phys.* **22** (6), 063015.

Davidson, P. A. 2004 *Turbulence: An Introduction for Scientists and Engineers*. Oxford Univ. Pr.

Dhruva, B., Tsuji, Y. & Sreenivasan, K. R. 1997 Transverse structure functions in high-Reynolds-number turbulence. *Phys. Rev. E.* **56** (5), R4928.

Eisma, J., Westerweel, J., Ooms, G. & Elsinga, G. E. 2015 Interfaces and internal layers in a turbulent boundary layer. *Phys. Fluids* **27** (5), 055103.

Elsinga, G. E., Ishihara, T., Goudar, M. V., da Silva, C. B. & Hunt, J. C. R. 2017 The scaling of straining motions in homogeneous isotropic turbulence. *J. Fluid Mech.* **829**, 31–64.

Elsinga, G. E. & Marusic, I. 2010 Universal aspects of small-scale motions in turbulence. *J. Fluid Mech.* **662**, 514–539.

Elsinga, G. E. & Marusic, I. 2016 The anisotropic structure of turbulence and its energy spectrum. *Phys. Fluids* **28** (1), 011701.

Enoki, R., Watanabe, T. & Nagata, K. 2023 Statistical properties of shear and nonshear velocity components in isotropic turbulence and turbulent jets. *Phys. Rev. Fluids* **8** (10), 104602.

Fiscaletti, D., Buxton, O. R. H. & Attili, A. 2021 Internal layers in turbulent free-shear flows. *Phys. Rev. Fluids* **6** (3), 034612.

Frisch, U., Sulem, P.-L. & Nelkin, M. 1978 A simple dynamical model of intermittent fully developed turbulence. *J. Fluid Mech.* **87** (4), 719–736.

Ganapathisubramani, B., Lakshminarasimhan, K. & Clemens, N. T. 2008 Investigation of three-dimensional structure of fine scales in a turbulent jet by using cinematographic stereoscopic particle image velocimetry. *J. Fluid Mech.* **598**, 141–175.

Gauding, M., Bode, M., Brahami, Y., Varea, É. & Danaila, L. 2021 Self-similarity of turbulent jet flows with internal and external intermittency. *J. Fluid Mech.* **919**, A41.

Ghira, A. A., Elsinga, G. E. & da Silva, C. B. 2022 Characteristics of the intense vorticity structures in isotropic turbulence at high Reynolds numbers. *Phys. Rev. Fluids* **7** (10), 104605.

Goto, S., Saito, Y. & Kawahara, G. 2017 Hierarchy of antiparallel vortex tubes in spatially periodic turbulence at high Reynolds numbers. *Phys. Rev. Fluids* **2** (6), 064603.

Gotoh, T., Fukayama, D. & Nakano, T. 2002 Velocity field statistics in homogeneous steady turbulence obtained using a high-resolution direct numerical simulation. *Phys. Fluids* **14** (3), 1065–1081.

Goudar, M. V. & Elsinga, G. E. 2018 Tracer particle dispersion around elementary flow patterns. *J. Fluid Mech.* **843**, 872–897.

Hayashi, M., Watanabe, T. & Nagata, K. 2021*a* Characteristics of small-scale shear layers in a temporally evolving turbulent planar jet. *J. Fluid Mech.* **920**, A38.

Hayashi, M., Watanabe, T. & Nagata, K. 2021*b* The relation between shearing motions and the turbulent/non-turbulent interface in a turbulent planar jet. *Phys. Fluids* **33** (5), 055126.

Hirota, .M, Nishio, Y., Izawa, S. & Fukunishi, Y. 2017 Vortex stretching in a homogeneous isotropic turbulence **822** (1), 012041.

Isaza, J. C., Salazar, R. & Warhaft, Z. 2014 On grid-generated turbulence in the near-and far field regions. *J. Fluid Mech.* **753**, 402–426.

Iyer, K. P., Sreenivasan, K. R. & Yeung, P. K. 2020 Scaling exponents saturate in three-dimensional isotropic turbulence. *Phys. Rev. Fluids* **5** (5), 054605.

Jiménez, J., Wray, A. A., Saffman, P. G. & Rogallo, R. S. 1993 The structure of intense vorticity in isotropic turbulence. *J. Fluid Mech.* **255**, 65–90.

Johnsen, E., Larsson, J., Bhagatwala, A. V., Cabot, W. H., Moin, P., Olson, B. J., Rawat, P. S., Shankar, S. K., Sjögreen, B., Yee, H. C., Zhong, X. & Lele, S. K. 2010 Assessment of high-resolution methods for numerical simulations of compressible turbulence with shock waves. *J. Comput. Phys.* **229** (4), 1213–1237.

Kailasnath, P., Sreenivasan, K. R. & Stolovitzky, G. 1992 Probability density of velocity increments in turbulent flows. *Phys. Rev. Lett.* **68** (18), 2766.

Kang, S.-J., Tanahashi, M. & Miyauchi, T. 2007 Dynamics of fine scale eddy clusters in turbulent channel flows. *J. Turbul.* **8**, N52.

Keylock, C. J. 2018 The Schur decomposition of the velocity gradient tensor for turbulent flows. *J. Fluid Mech.* **848**, 876–905.

Kistler, A. L. & Vrebalovich, T. 1966 Grid turbulence at large Reynolds numbers. *J. Fluid Mech.* **26** (1), 37–47.

Kitamura, T., Nagata, K., Sakai, Y., Sasoh, A., Terashima, O., Saito, H. & Harasaki, T. 2014 On invariants in grid turbulence at moderate Reynolds numbers. *J. Fluid Mech.* **738**, 378–406.

Kolář, V. 2007 Vortex identification: New requirements and limitations. *Int. J. Heat Fluid Flow* **28** (4), 638–652.

Kolář, V. & Šístek, J. 2014 Recent progress in explicit shear-eliminating vortex identification. In *Proceedings of the 19th Australasian Fluid Mechanics Conference*.

Kolmogorov, A. N. 1941 The local structure of turbulence in incompressible viscous fluid for very large Reynolds numbers. *Dokl. Akad. Nauk SSSR* **30**, 299–303.

Kolmogorov, A. N. 1962 A refinement of previous hypotheses concerning the local structure of turbulence in a viscous incompressible fluid at high Reynolds number. *J. Fluid Mech.* **13** (1), 82–85.

Kouchi, T., Fukuda, S., Miyai, S., Nagata, Y. & Yanase, S. 2019 Acetone-condensation nano-particle image velocimetry in a supersonic boundary layer. In *AIAA Scitech 2019 Forum*, p. 1821.

Krogstad, P.-Å. & Davidson, P. A. 2012 Near-field investigation of turbulence produced by multi-scale grids. *Phys. Fluids* **24** (3), 035103.

Kronborg, J. & Hoffman, J. 2023 The triple decomposition of the velocity gradient tensor as a standardized real Schur form. *Phys. Fluids* **35** (3), 031703.

Leung, T., Swaminathan, N. & Davidson, P. A. 2012 Geometry and interaction of structures in homogeneous isotropic turbulence. *J. Fluid Mech.* **710**, 453–481.

Lin, S. J. & Corcos, G. M. 1984 The mixing layer: deterministic models of a turbulent flow. Part 3. The effect of plane strain on the dynamics of streamwise vortices. *J. Fluid Mech.* **141**, 139–178.

Liu, C., Gao, Y., Tian, S. & Dong, X. 2018 Rortex-A new vortex vector definition and vorticity tensor and vector decompositions. *Phys. Fluids* **30** (3), 035103.

Lundgren, T. S. 1993 A small-scale turbulence model. *Phys. Fluids* **5** (6), 1472–1483.

Marusic, I. & Monty, J. P. 2019 Attached eddy model of wall turbulence. *Annu. Rev. Fluid Mech.* **51**, 49–74.

Matsuda, K., Schneider, K. & Yoshimatsu, K. 2021 Scale-dependent statistics of inertial particle distribution in high Reynolds number turbulence. *Phys. Rev. Fluids* **6** (6), 064304.

Matsushima, T., Nagata, K. & Watanabe, T. 2021 Wavelet analysis of shearless turbulent mixing layer. *Phys. Fluids* **33** (2).

Melina, G., Bruce, P. J. K. & Vassilicos, J. C. 2016 Vortex shedding effects in grid-generated turbulence. *Phys. Rev. Fluids* **1** (4), 044402.

Mohamed, M. S. & Larue, J. C. 1990 The decay power law in grid-generated turbulence. *J. Fluid Mech.* **219**, 195–214.

Mori, T., Watanabe, T. & Nagata, K. 2024 Nearly homogeneous and isotropic turbulence generated by the interaction of supersonic jets. *Exp. Fluids* **65** (4), 47.

Morinishi, Y., Lund, T. S., Vasilyev, O. V. & Moin, P. 1998 Fully conservative higher order finite difference schemes for incompressible flow. *J. Comput. Phys.* **143** (1), 90–124.

Mouri, H., Hori, A. & Kawashima, Y. 2007 Laboratory experiments for intense vortical structures in turbulence velocity fields. *Phys. Fluids* **19** (5), 055101.

Nagata, K., Saiki, T., Sakai, Y., Ito, Y. & Iwano, K. 2017 Effects of grid geometry on non-equilibrium dissipation in grid turbulence. *Phys. Fluids* **29** (1).

Nagata, R., Watanabe, T., Nagata, K. & da Silva, C. B. 2020*a* Triple decomposition of velocity gradient tensor in homogeneous isotropic turbulence. *Comput. Fluids* **198**, 104389.

Nagata, T., Noguchi, A., Kusama, K., Nonomura, T., Komuro, A., Ando, A. & Asai, K. 2020*b* Experimental investigation on compressible flow over a circular cylinder at Reynolds number of between 1000 and 5000. *J. Fluid Mech.* **893**, A13.

Naso, A. & Pumir, A. 2005 Scale dependence of the coarse-grained velocity derivative tensor structure in turbulence. *Phys. Rev. E* **72** (5), 056318.

Neamtu-Halic, M. M., Mollicone, J.-P., Van Reeuwijk, M. & Holzner, M. 2021 Role of vortical structures for enstrophy and scalar transport in flows with and without stable stratification. *J. Turbul.* **22** (7), 393–412.

Nieuwstadt, F. T .and Westerweel, J. & Boersma, B. 2016 *Introduction to Theory and Applications of Turbulent Flows*. Springer.

Pack, D. C. 1950 A note on Prandtl's formula for the wave-length of a supersonic gas jet. *Q. J. Mech. Appl. Math.* **3** (2), 173–181.

Perry, A. E. & Chong, M. S. 1994 Topology of flow patterns in vortex motions and turbulence. *Appl. Sci. Res.* **53**, 357–374.

Pirozzoli, S., Bernardini, M. & Grasso, F. 2010 On the dynamical relevance of coherent vortical structures in turbulent boundary layers. *J. Fluid Mech.* **648**, 325–349.

Pizzaia, A. & Rossmann, T. 2018 Effect of boundary layer thickness on transverse sonic jet mixing in a supersonic turbulent crossflow. *Phys. Fluids* **30** (11).

Pope, S. B. 2000 *Turbulent Flows*. Cambridge Univ. Pr.

Rabey, P. K., Wynn, A. & Buxton, O. R. H. 2015 The kinematics of the reduced velocity gradient tensor in a fully developed turbulent free shear flow. *J. Fluid Mech.* **767**, 627–658.

Saddoughi, S. G. & Veeravalli, S. V. 1994 Local isotropy in turbulent boundary layers at high Reynolds number. *J. Fluid Mech.* **268**, 333–372.

Sakurai, Y. & Ishihara, T. 2018 Relationships between small-scale fluid motions and inertial particle clustering in turbulence. *J. Phys. Soc. Japan* **87** (9), 093401.

Saw, E.-W., Debue, P., Kuzzay, D., Daviaud, F. & Dubrulle, B. 2018 On the universality of anomalous scaling exponents of structure functions in turbulent flows. *J. Fluid Mech.* **837**, 657–669.

She, Z.-S. & Leveque, E. 1994 Universal scaling laws in fully developed turbulence. *Phys. Rev. Lett.* **72** (3), 336.

Shtilman, L., Spector, M. & Tsinober, A. 1993 On some kinematic versus dynamic properties of homogeneous turbulence. *J. Fluid Mech.* **247**, 65–77.

da Silva, C. B., Dos Reis, R. J. N. & Pereira, J. C. F. 2011 The intense vorticity structures near the turbulent/non-turbulent interface in a jet. *J. Fluid Mech.* **685**, 165–190.

Sreenivasan, K. R. & Antonia, R. A. 1997 The phenomenology of small-scale turbulence. *Annu. Rev. Fluid Mech.* **29** (1), 435–472.

Takamure, K., Kato, H. & Uchiyama, T. 2023 Wake characteristics of sphere with circular uniaxial through-hole arranged perpendicularly to streamwise direction. *Powder Technol.* **415**, 118175.

Tan, S., Xu, X., Qi, Y. & Ni, R. 2023 Scalings and decay of homogeneous, nearly isotropic turbulence behind a jet array. *Phys. Rev. Fluids* **8** (2), 024603.

Tang, S. L., Antonia, R. A., Djenidi, L., Danaila, L. & Zhou, Y. 2017 Finite Reynolds number effect on the scaling range behaviour of turbulent longitudinal velocity structure functions. *J. Fluid Mech.* **820**, 341–369.

Theunissen, R. 2010 Adaptive image interrogation for PIV: Application to compressible flows and interfaces. *Ph.D. thesis, TU Delft, Delft University of Technology, Delft, The Netherlands.* .

Thormann, A. & Meneveau, C. 2014 Decay of homogeneous, nearly isotropic turbulence behind active fractal grids. *Phys. Fluids* **26**, 025112.

Townsend, A. A. 1976 *The structure of turbulent shear flow*. Cambridge Univ. Pr.

Tsinober, A. 2009 *An informal conceptual introduction to turbulence*. Springer.

Vincent, A. & Meneguzzi, M. 1994 The dynamics of vorticity tubes in homogeneous turbulence. *J. Fluid Mech.* **258**, 245–254.

Wang, Y., Gao, Y. & Liu, C. 2018 Galilean invariance of Rortex. *Phys. Fluids* **30** (11), 111701.

Watanabe, T. 2024 Efficient enhancement of turbulent entrainment by small-scale shear instability. *J. Fluid Mech.* **988**, A20.

Watanabe, T., Jaulino, R., Taveira, R. R., da Silva, C. B., Nagata, K. & Sakai, Y. 2017 Role of an isolated eddy near the turbulent/non-turbulent interface layer. *Phys. Rev. Fluids* **2** (9), 094607.

Watanabe, T. & Nagata, K. 2018 Integral invariants and decay of temporally developing grid turbulence. *Phys. Fluids* **30** (10), 105111.

Watanabe, T. & Nagata, K. 2022 Energetics and vortex structures near small-scale shear layers in turbulence. *Phys. Fluids* **34** (9), 095114.

Watanabe, T. & Nagata, K. 2023 The response of small-scale shear layers to perturbations in turbulence. *J. Fluid Mech.* **963**, A31.

Watanabe, T., Riley, J. J., Nagata, K., Onishi, R. & Matsuda, K. 2018 A localized turbulent mixing layer in a uniformly stratified environment. *J. Fluid Mech.* **849**, 245–276.

Watanabe, T., Tanaka, K. & Nagata, K. 2020 Characteristics of shearing motions in incompressible isotropic turbulence. *Phys. Rev. Fluids* **5** (7), 072601(R).

Westerweel, J. & Scarano, F. 2005 Universal outlier detection for PIV data. *Exp. Fluids* **39** (6), 1096–1100.

Zheng, Y., Nagata, K. & Watanabe, T. 2021 Turbulent characteristics and energy transfer in the far field of active-grid turbulence. *Phy. Fluids* **33** (11), 115119.